

Protostellar-disc fragmentation across all metallicities

Ryoki Matsukoba,^{1,2}★ Kei E. I. Tanaka,^{3,4} Kazuyuki Omukai,¹ Eduard I. Vorobyov⁵ and Takashi Hosokawa²

¹*Astronomical Institute, Graduate School of Science, Tohoku University, Aoba, Sendai 980-8578, Japan*

²*Department of Physics, Graduate School of Science, Kyoto University, Sakyo, Kyoto 606-8502, Japan*

³*Center for Astrophysics and Space Astronomy, University of Colorado Boulder, Boulder, CO 80309, USA*

⁴*National Astronomical Observatory of Japan, National Institutes of Natural Sciences, 2-21-1 Osawa, Mitaka, Tokyo 181-8588, Japan*

⁵*Department of Astrophysics, University of Vienna, Vienna, 1180, Austria*

Accepted XXX. Received YYY; in original form ZZZ

ABSTRACT

Cosmic metallicity evolution possibly creates the diversity of star formation modes at different epochs. Gravitational fragmentation of circumstellar discs provides an important formation channel of multiple star systems, including close binaries. We here study the nature of disc fragmentation, systematically performing a suite of two-dimensional radiation-hydrodynamic simulations, in a broad range of metallicities, from the primordial to the solar values. In particular, we follow relatively long-term disc evolution over 15 kyr after the disc formation, incorporating the effect of heating by the protostellar irradiation. Our results show that the disc fragmentation occurs at all metallicities $1-0\ Z_{\odot}$, yielding self-gravitating clumps. Physical properties of the clumps, such as their number and mass distributions, change with the metallicity due to different gas thermal evolution. For instance, the number of clumps is the largest for the intermediate metallicity range of $10^{-2}-10^{-5}\ Z_{\odot}$, where the dust cooling is effective exclusively in a dense part of the disc and causes the fragmentation of spiral arms. The disc fragmentation is more modest for $1-0.1\ Z_{\odot}$ thanks to the disc stabilization by the stellar irradiation. Such metallicity dependence agrees with the observed trend that the close binary fraction increases with decreasing metallicity in the range of $1-10^{-3}\ Z_{\odot}$.

Key words: accretion, accretion discs – hydrodynamics – methods: numerical – stars: formation – stars: protostars

1 INTRODUCTION

Stars in the contemporary and early universe differ in the mass. Those in the local universe at the solar metallicity have a peak in the initial mass function at $\lesssim 1\ M_{\odot}$ (Kroupa 2002; Chabrier 2003; Bastian et al. 2010), while first stars forming from the primordial gas (or Pop III stars) have much higher masses of $\sim 10-100\ M_{\odot}$ according to numerical simulations (e.g. Hirano et al. 2014, 2015; Susa et al. 2014). This indicates that the typical stellar mass has been changing over cosmic time along with the accumulation of metals in a star-forming gas. Some metallicity-dependent star-formation processes must have caused this transition.

One such process is gravitational fragmentation of a prestellar cloud. Theories tell that just a little bit of metals and dust grains in a star-forming gas make a big difference in this regard. Semi-analytical models predict that those clouds are vulnerable to fragmentation provided the metallicity is $\gtrsim 10^{-5}\ Z_{\odot}$ owing to the dust cooling operating at densities $> 10^{10}\ \text{cm}^{-3}$ (Omukai 2000; Schneider et al. 2003, 2006; Omukai et al. 2005, 2010; Chiaki et al. 2014, 2015). Numerical simulations demonstrate that the cloud fragmentation indeed occurs, forming low-mass clumps with $\sim 0.01\ M_{\odot}$, unlike in the case of $0\ Z_{\odot}$ (Clark et al. 2008; Dopcke et al. 2011, 2013; Meece et al. 2014; Smith et al. 2015; Chiaki et al. 2016; Safrank-Shrader et al. 2016).

This enables the formation of low-mass ($\lesssim 1\ M_{\odot}$) stars in the early universe.

Fragmentation takes place also in a later stage of star formation after the birth of a protostar; in a circumstellar disc (Kratter & Lodato 2016). A disc accreting gas from the surrounding envelope tends to fragment by gravitational instability, producing self-gravitating clumps. Some numerical simulations of Pop III star formation report the formation of low-mass clumps with $\sim 0.1-1\ M_{\odot}$ as a result of the disc fragmentation (e.g. Machida et al. 2008; Stacy et al. 2010; Clark et al. 2011; Greif et al. 2012; Machida & Doi 2013; Vorobyov et al. 2013; Hosokawa et al. 2016; Stacy et al. 2016; Hirano & Bromm 2017; Riaz et al. 2018; Susa 2019; Sharda et al. 2020; Sugimura et al. 2020; Wollenberg et al. 2020; Kimura et al. 2021; Prole et al. 2022). The disc fragmentation is also supposed to provide a channel for binary and planet formation in the present-day star formation (e.g. Zhao et al. 2020, and references therein). Understanding metallicity dependence of the disc fragmentation is thus a clue to bridge the gap between star formation in the early and contemporary universe. Tanaka & Omukai (2014) studied the metallicity dependence of the disc fragmentation using a one-dimensional disc model assuming steady accretion. They predicted that discs are most vulnerable to gravitational fragmentation in a metallicity range of $10^{-3}-10^{-5}\ Z_{\odot}$ due to efficient dust cooling.

Observations also support the idea that low metallicity discs are more prone to fragment. Moe et al. (2019) reported that the close binary fraction (separation less than 10 au) of solar-type stars inversely

★ E-mail: r.matsukoba@tap.scphys.kyoto-u.ac.jp

correlates with the metallicity at $-3 < [\text{Fe}/\text{H}] < 0$. Although difficult to statistically examine the binary fraction at lower metallicities, [Schlaufman et al. \(2018\)](#) reported the discovery of a close binary with $[\text{Fe}/\text{H}] = -4.07$. The disc fragmentation is a plausible mechanism to form such close binary systems.

Self-gravitational hydrodynamics simulations are powerful tools to study metallicity dependence of the disc fragmentation, and have demonstrated that the disc fragmentation is intense at metallicities 10^{-3} – $10^{-5} Z_{\odot}$ ([Machida & Nakamura 2015](#); [Chon et al. 2021](#); [Shima & Hosokawa 2021](#); [Chiaki & Yoshida 2022](#)), as predicted by [Tanaka & Omukai \(2014\)](#). Those previous studies, however, still have the following limitations. For example, the metallicity range considered differs in different studies; 1 – $10^{-2} Z_{\odot}$ in [Vorobyov et al. \(2020b\)](#) and 10^{-3} – $0 Z_{\odot}$ in [Shima & Hosokawa \(2021\)](#) and [Chiaki & Yoshida \(2022\)](#). The limited range of metallicity studied hinders thorough understanding of the difference in the star formation in the early and contemporary universe. Although [Machida & Nakamura \(2015\)](#)'s calculation covered a wider metallicity range of 1 – $0 Z_{\odot}$, they followed the evolution only up to ~ 100 yr after the protostar formation, far shorter than the entire duration of accretion, $\sim 10^5$ yr. [Chon et al. \(2021\)](#) followed longer-term ($\sim 10^5$ yr) evolution in a metallicity range of 0.1 – $10^{-6} Z_{\odot}$, without incorporating the disc irradiation heating from the accreting protostars, which effectively stabilizes the disc, as known for the solar-metallicity case ([Matzner & Levin 2005](#); [Vorobyov & Basu 2010](#)).

In this work, we systematically study the metallicity dependence of the disc fragmentation beyond the limitations of the previous studies. We consider the cases with different metallicities of the full coverage, 1 – $0 Z_{\odot}$. We follow the long-term evolution for 15 kyr after the disc formation, using two-dimensional radiation-hydrodynamic simulations, where we consistently solve the gas thermal evolution affected by the stellar irradiation heating. To see the metallicity dependence quantitatively, we analyze physical properties of self-gravitating clumps produced by disc fragmentation, such as their number and mass distributions for each case.

The structure of the rest of the paper is as follows. We describe our simulation method in Section 2. We present the basic results in Section 3, where we clarify metallicity dependence of the disc fragmentation. We provide discussion and summary in Section 4 and Section 5, respectively.

2 METHOD

We perform a suite of two-dimensional simulations integrating the vertical structure of a disc. In what follows, we briefly describe the method for the self-gravitational radiation-hydrodynamic simulations and our initial conditions. Further details are also provided in [Vorobyov et al. \(2020a,b\)](#).

2.1 Two-dimensional self-gravitational radiation-hydrodynamic simulations

We use polar-coordinate (r, ϕ) grids with 512×512 spatial zones as a default setting. The grids are logarithmically spaced in the radial direction and have equal spacing in the azimuthal direction. A sink cell with the radius of 5 au is introduced at the centre of the computational domain. The position of the outer boundary varies according to different models as described in Section 2.2.

To follow the time evolution of the gas surface density, velocity, and temperature, we solve the vertically-integrated equations of

continuity, motion, and energy transport:

$$\frac{\partial \Sigma}{\partial t} = -\nabla \cdot (\Sigma \mathbf{u}), \quad (1)$$

$$\frac{\partial}{\partial t} (\Sigma \mathbf{u}) + \nabla \cdot (\Sigma \mathbf{u} \otimes \mathbf{u}) = -\nabla P + \Sigma \mathbf{g} + \nabla \cdot \mathbf{\Pi}, \quad (2)$$

$$\frac{\partial e}{\partial t} + \nabla \cdot (e \mathbf{u}) = -P (\nabla \cdot \mathbf{u}) - Q_{\text{tot}} + (\nabla \mathbf{u}) : \mathbf{\Pi}, \quad (3)$$

where Σ is the gas surface density, $\mathbf{u} = u_r \hat{\mathbf{r}} + u_{\phi} \hat{\boldsymbol{\phi}}$ is the planar velocity, P is the vertically-integrated gas pressure, $\nabla = \hat{\mathbf{r}} \partial / \partial r + \hat{\boldsymbol{\phi}} r^{-1} \partial / \partial \phi$ is the derivative operator, $\mathbf{g} = g_r \hat{\mathbf{r}} + g_{\phi} \hat{\boldsymbol{\phi}}$ is the gravitational acceleration, e is the internal energy per unit area, Q_{tot} is the total cooling rate per unit area, and $\mathbf{\Pi}$ is the viscous stress tensor.

The gas pressure and internal energy are related by the ideal-gas equation of state,

$$P = (\gamma - 1)e, \quad (4)$$

with the adiabatic exponent γ . The viscous stress tensor is

$$\mathbf{\Pi} = 2\Sigma\nu \left[\nabla \mathbf{u} - \frac{1}{3} (\nabla \cdot \mathbf{u}) \mathbf{e} \right], \quad (5)$$

where \mathbf{e} is the unit tensor and ν is the kinematic viscosity, which is given according to the α description ([Shakura & Sunyaev 1973](#)). We set $\alpha = 10^{-4}$ uniformly in the space to account for residual turbulence in the disc midplane owing possibly to the magnetorotational instability at the surface layers of the disc. We note that the gravitational torque, rather than the viscosity, dominates the angular momentum transfer in our simulations, as is the case for solar-metallicity protostellar discs in their early stages of evolution ([Vorobyov & Basu 2009](#)). The self-gravitational potential created by the gas is

$$\begin{aligned} \Phi_{\text{gas}}(r, \phi) = & -G \int_{r_{\text{sc}}}^{r_{\text{out}}} r' dr' \\ & \times \int_0^{2\pi} \frac{\Sigma(r', \phi')}{\sqrt{r'^2 + r^2 - 2rr' \cos(\phi' - \phi)}} d\phi', \end{aligned} \quad (6)$$

where G is the gravitational constant, and r_{sc} is the sink radius of 5 au. The gravitational acceleration by the gas potential is

$$\mathbf{g}_{\text{gas}} = -\nabla \Phi_{\text{gas}}(r, \phi). \quad (7)$$

We assume that the sink cell represents a single central star accreting the gas. The gravitational acceleration by the central star with the mass M_* is

$$\mathbf{g}_{\text{star}} = -\frac{GM_*}{r^2} \hat{\mathbf{r}}. \quad (8)$$

The sum of the two components gives the gravitational acceleration, i.e. $\mathbf{g} = \mathbf{g}_{\text{gas}} + \mathbf{g}_{\text{star}}$. We assume hydrostatic equilibrium in the direction perpendicular to the r – ϕ plane everywhere ([Vorobyov & Basu 2009](#)):

$$\rho c_s^2 = \frac{\pi}{2} G \Sigma^2 + \frac{2GM_{\text{star}} \rho}{r} \left[1 - \left(1 + \frac{\Sigma}{2\rho r} \right)^{-1/2} \right], \quad (9)$$

where ρ is the mass density, and c_s is the sound speed defined as

$$c_s = \sqrt{\gamma \frac{k_B T}{\mu m_H}}, \quad (10)$$

where k_B is the Boltzmann constant, T is the gas temperature, μ is the mean molecular weight, and m_H is the mass of a hydrogen nucleus.

The total cooling rate is the sum of the contribution by each process as follows ([Vorobyov et al. 2020a](#)):

$$Q_{\text{tot}} = Q_{\text{cont,gas}} + Q_{\text{cont,dust}} + Q_{\text{mole}} + Q_{\text{metal}} + Q_{\text{chem}}, \quad (11)$$

where $Q_{\text{cont,gas}}$ and $Q_{\text{cont,dust}}$ are the rates by continuum emission of gas and dust, Q_{mole} by line emission of H_2 and HD molecules, Q_{metal} by fine-structure line emission of O I (63 μm) and C II (158 μm), and Q_{chem} is the chemical cooling rate. The dust continuum term $Q_{\text{cont,dust}}$ represents the process by which the energy of the gas is transferred to the dust grains by collision and released into the radiation field. This process acts as cooling for the gas when the gas temperature is higher than the dust temperature, while as heating otherwise. We evaluate the dust temperature T_d by solving the energy balance between the photon absorption and emission at the dust surface and collisional energy exchange with the gas (Omukai et al. 2010; Vorobyov et al. 2020a):

$$\kappa_{\text{p,d}} B(T_d) = \kappa_{\text{p,d}} J + \Gamma_{\text{coll}}, \quad (12)$$

where $\kappa_{\text{p,d}}$ is the Planck mean opacity for dust grains, $B(T_d) = \sigma_{\text{SB}} T_d^4 / \pi$ is the intensity for the black body at T_d with the Stefan-Boltzmann constant σ_{SB} , J is the mean intensity, which includes the effects of the central stellar irradiation and uniform background radiation, and Γ_{coll} is the heating rate of dust through collisions with gas particles (Hollenbach & McKee 1979). Note the collisional heating for dust grains is cooling for the gas. We calculate the Planck mean opacity $\kappa_{\text{p,d}}$ using the table given in Semenov et al. (2003). The chemical cooling term can also be negative, in this case it works as heating. The terms $Q_{\text{cont,dust}}$ and Q_{metal} are proportional to the metallicity in the optically thin regime. We note that the photon trapping effect for these cooling terms is also considered by evaluating the optical depth through the disc as in Vorobyov et al. (2020a).

In self-gravitational hydrodynamic simulations, artificial fragmentation can be triggered if the Jeans length l_J is only poorly resolved with less than 4 grid cells:

$$4x_{\text{grid}} > l_J = \sqrt{\frac{\pi c_s^2}{G\rho}}, \quad (13)$$

where x_{grid} is the grid size (Truelove et al. 1997). Subsequent studies also suggest that even higher resolution is necessary to capture the gravity-driven turbulence (e.g. Federrath et al. 2011; Lichtenberg & Schleicher 2015). To prevent the artificial fragmentation, we suppress cooling by multiplying the total rate Q_{tot} by a function:

$$C_{\text{limit}} = \begin{cases} \exp\left[-\left(\frac{\xi-1}{0.1}\right)^2\right] & (\xi \geq 1), \\ 1 & (\xi < 1), \end{cases} \quad (14)$$

$$\xi = f_{\text{limit}} \frac{x_{\text{grid}}}{l_J}, \quad (15)$$

where f_{limit} is an arbitrary coefficient (Hosokawa et al. 2016), which is 6 in this study. The function C_{limit} becomes smaller than 1 where the Jeans length is shorter than six times the grid size, reducing the cooling rate and preventing artificial fragmentation.

We assume that the central star accretes the gas flowing into the sink cell at each time step. We consider the irradiation by the accreting protostar, which contributes to the disc stabilization by increasing the dust and gas temperatures (see Equation 12 and Section 4.1). The protostellar luminosity consists of two components; accretion luminosity and stellar intrinsic luminosity. We evaluate the intrinsic luminosity from pre-calculated stellar evolutionary tracks. While Vorobyov et al. (2020b) use the tracks obtained by the STELLAR code (Yorke & Bodenheimer 2008), we use the tracks calculated as in Hosokawa & Omukai (2009) for all the metallicities we consider. Our tracks for 10^{-2} , 10^{-3} , and $0 Z_{\odot}$ are identical to those used in Fukushima et al. (2020). The evolutionary tracks provide the stellar radius and intrinsic luminosity as functions of the stellar mass

and accretion rate. We use the time-averaged accretion rate for the previous five years because it fluctuates significantly in time.

We also add a uniform background radiation field over the entire computational domain, which imposes a floor temperature. The background radiation is assumed to be 10 K, the temperature of the cosmic microwave background at the redshift of $z = 3$. The floor temperature is reached only for the cases of $1-10^{-2} Z_{\odot}$ in our simulations.

We solve the non-equilibrium chemical network of 8 species H, H_2 , H^+ , H^- , D, HD, D^+ , and e^- with 27 reactions (see Vorobyov et al. 2020a). We define the chemical fraction as $y(i) \equiv n(i)/n_{\text{H}}$, where $n(i)$ and n_{H} are the number densities of a species i and the hydrogen nuclei, respectively. We assume neutrality for helium, and its chemical fraction is $y(\text{He}) = 8.333 \times 10^{-2}$. The deuterium fraction is $y(\text{D}) = 3 \times 10^{-5}$. We adopt the standard values of the metal contents in the solar neighbourhood for the case of $1 Z_{\odot}$; $y(\text{C}) = 9.27 \times 10^{-5}$ and $y(\text{O}) = 3.57 \times 10^{-4}$. These values both linearly scale with decreasing metallicity. We also assume that all the carbon and oxygen nuclei always exist as C^+ ions and O atoms. Regarding dust grains, we use the standard composition and size distributions in the Galactic interstellar medium (Mathis et al. 1977). We make the gas-dust mass ratio vary in proportion to the metallicity.

2.2 Initial conditions and setups

We start the simulation from a prestellar cloud core. We make the core gravitationally unstable to initiate the collapse. It takes about twice the free-fall time for a circumstellar disc to appear when the centrifugal radius of the accreting gas exceeds the sink radius. We study the degree of the disc fragmentation through the subsequent evolution at a given metallicity.

The initial core profile has a plateau with a uniform surface density around the centre (Vorobyov & Basu 2010):

$$\Sigma = \frac{\Sigma_0}{\sqrt{1 + (r/r_0)^2}}, \quad (16)$$

$$\Omega = 2\Omega_0 \left(\frac{r_0}{r}\right)^2 \left[\sqrt{1 + \left(\frac{r}{r_0}\right)^2} - 1 \right], \quad (17)$$

where Σ_0 is the surface density at the plateau, Ω_0 is the angular velocity at the plateau, and r_0 is the plateau radius. The above profile emerges when an axisymmetric cloud gravitationally collapses with constant angular momentum (Basu 1997). The plateau radius r_0 is proportional to the Jeans length

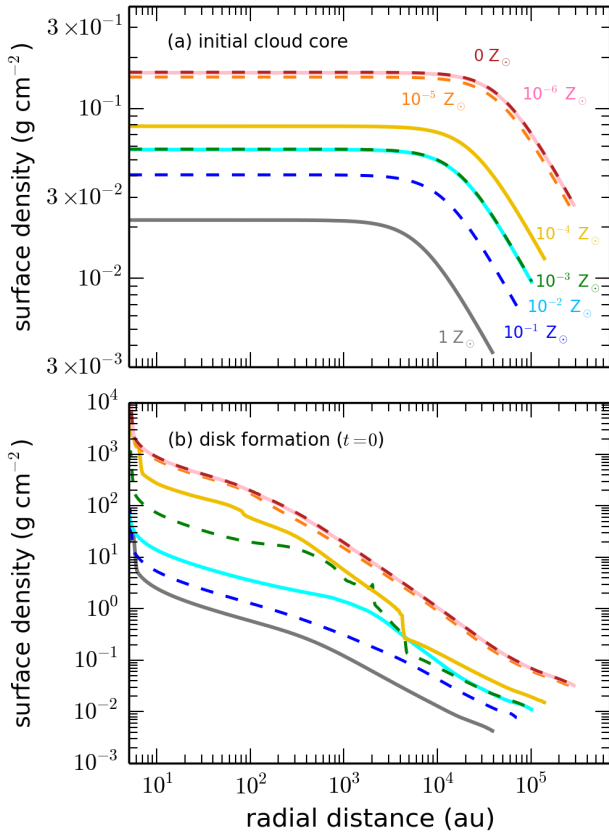
$$r_0 = A \frac{c_{\text{s},0}}{\sqrt{\pi G \rho_0}}, \quad (18)$$

where A is a constant parameter, $c_{\text{s},0}$ is the initial sound speed, and $\rho_0 = 2.2 \times 10^{-19} \text{ g cm}^{-3}$ is the initial mass density ($n_{\text{H},0} = 10^5 \text{ cm}^{-3}$ in the number density). The initial mass and the plateau surface densities are related as $\Sigma_0 = r_0 \rho_0$. The constant A is a parameter defining the initial density perturbation. We set $A = \sqrt{1.2}$, with which the ratio of the cloud thermal and gravitational energies is 0.77 for all the cases. We also set the ratio of the rotational and gravitational energies as 0.01 by adjusting the plateau angular velocity Ω_0 .

Table 1 summarizes the models with different metallicities we consider. To determine the initial gas temperature and chemical fractions, both of which depend on the metallicity, we use a one-zone model developed by Omukai et al. (2005). We follow the evolution of the central density, temperature, and chemical fractions of a collapsing core until the central density reaches $n_{\text{H},0} = 10^5 \text{ cm}^{-3}$. We assign

Table 1. The initial properties of the prestellar cloud cores

metallicity Z_{\odot}	T_0 K	$c_{s,0}$ km s $^{-1}$	Σ_0 g cm $^{-2}$	r_0 pc	r_{out} pc	Ω_0 km s $^{-1}$ pc $^{-1}$	M_{cloud} M_{\odot}
1	10	0.19	0.022	0.032	0.19	0.60	3.4
10^{-1}	33	0.36	0.041	0.059	0.35	0.60	21
10^{-2}	43	0.51	0.057	0.083	0.50	0.60	60
10^{-3}	39	0.51	0.058	0.083	0.50	0.60	61
10^{-4}	72	0.70	0.079	0.11	0.68	0.60	160
10^{-5}	270	1.4	0.15	0.22	1.3	0.60	1200
10^{-6}	310	1.4	0.16	0.24	1.4	0.60	1400
0	310	1.4	0.16	0.24	1.4	0.60	1400

**Figure 1.** Radial profiles of the azimuthally-averaged surface density. The two panels show the snapshots at different epochs: (a) the initial states of the simulations, and (b) the disc formation, which is defined as $t = 0$ (see the text). The line colours represent the metallicities of 1 (black), 10^{-1} (blue), 10^{-2} (cyan), 10^{-3} (green), 10^{-4} (yellow), 10^{-5} (orange), 10^{-6} (pink), and $0 Z_{\odot}$ (red).

the values obtained by the one-zone model homogeneously to the entire computational domain. The outer boundary of the computational domain r_{out} is set as six times larger than the plateau radius r_0 , to ensure that the initial configuration is marginally unstable to gravitational collapse. We show the surface density profiles of the prestellar cloud obtained from Equation (16) in Figure 1a. The plateau surface density Σ_0 is smaller with higher metallicity because the initial sound speed and thus the plateau radius are smaller. We can calculate the total cloud mass M_{cloud} by using the initial surface density profile,

i.e. ranging from the smallest value of $3.4 M_{\odot}$ at $1 Z_{\odot}$ to the largest $1400 M_{\odot}$ at $0 Z_{\odot}$ (Table 1).

As mentioned earlier in this section, the initial prestellar cloud gravitationally collapses, and then the circumstellar disc forms once the centrifugal radius of the infalling gas becomes larger than the sink cell radius of 5 au. Figure 1b shows the surface density profiles at the disc formation. We define the epoch of disc formation as $t = 0$, and then follow the evolution until $t = 15$ kyr. As shown below, the stellar mass exceeds $20 M_{\odot}$ by the end of the simulations in the cases of 10^{-5} , 10^{-6} , and $0 Z_{\odot}$ owing to high accretion rates. We do not incorporate the ionizing feedback from such massive stars, which disturbs the accretion flow and limits the stellar mass growth (McKee & Tan 2008; Hosokawa et al. 2011; Tanaka et al. 2018; Fukushima et al. 2020), for simplicity. If the ionizing feedback reduces the mass supply from the envelope to the disc by the epoch we consider, it likely works against disc fragmentation. Our current results hence correspond to the maximal effects of the disc fragmentation for the cases of $\leq 10^{-5} Z_{\odot}$.

3 METALLICITY DEPENDENCE OF DISC FRAGMENTATION

3.1 Disc fragmentation in 15 kyr since the disc formation

3.1.1 Fragmenting discs and self-gravitating clumps

This section presents the simulation results for all the cases listed in Table 1 and clarifies the metallicity dependence of disc fragmentation. In particular, we study the masses and number of clumps forming via disc fragmentation at each metallicity.

Figure 2 shows the spatial distribution of the surface density around the central star at $t = 15$ kyr after the disc formation. We see the clumpy structure for all the cases, suggesting that the disc fragmentation generally occurs by the epoch of the presented snapshots. The number of the clumps depends on the metallicity. In the case of $1 Z_{\odot}$, for example, only one clump is embedded within the spiral arm ~ 100 au away from the centre. On the other hand, at lower metallicities of $< 10^{-2} Z_{\odot}$, there are a large number of clumps, which prevent the buildup of a well-defined disc structure. These results indicate that the disc fragmentation is more vigorous at lower metallicities.

Figure 2 also shows that the spiral arms and clumps distribute over a broader area at lower metallicities. At $1 Z_{\odot}$, for example, the spatial extent of the spiral arms is limited to a small area of ≈ 200 au, whereas it covers a larger size of ~ 1000 au at $0 Z_{\odot}$. These differences originate from higher prestellar cloud temperatures (or higher sound speeds) at lower metallicity (see Table 1). The higher the sound speed, the broader range of the gas accretes onto the star-disc system by a

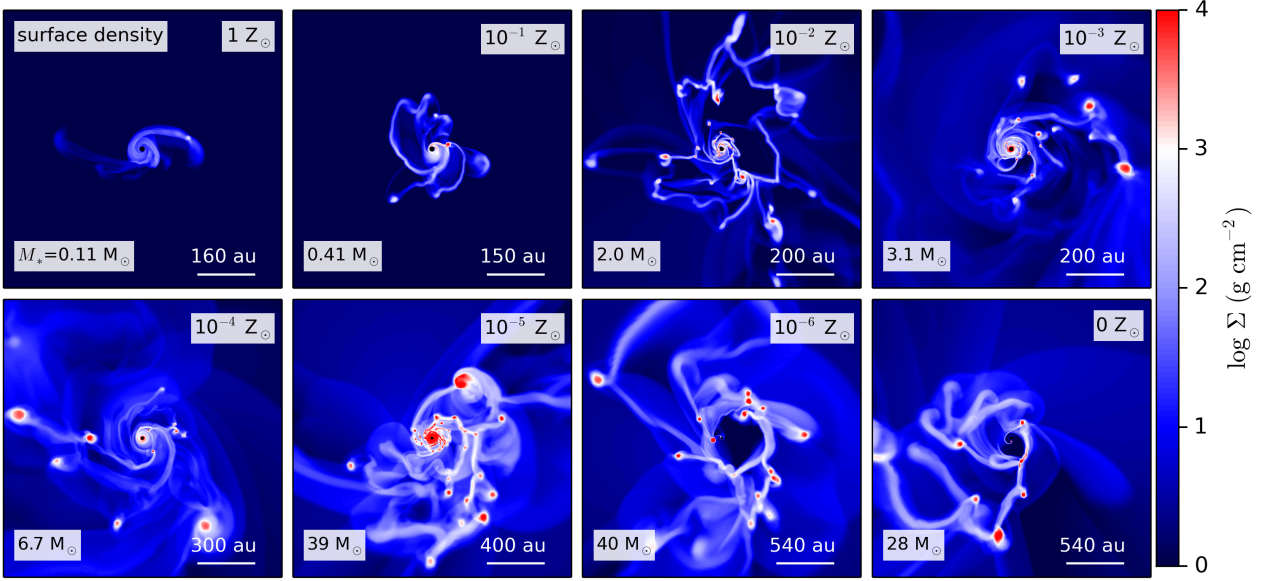


Figure 2. Spatial distributions of the surface density at the epoch of 15 kyr after the disc formation. The panels represent the cases of the different metallicities listed in Table 1. The mass of the central star is indicated in the lower-left corner of each panel. Note that the panel for the lower-metallicity case shows the broader area around the star.

given epoch, which provides a larger angular momentum. Therefore, the disc and spiral arms spread out faster with lower metallicities.

In general, high sound speed of the prestellar cloud $c_{s,0}$ leads to a high infall rate from the envelope onto the central disc-star system (see also Section 3.2), which is approximately described as

$$\dot{M}_{\text{infall}} \simeq \frac{M_J}{t_{\text{ff}}} \simeq \frac{c_s^3}{G}, \quad (19)$$

where $M_J = 4/3\pi\rho(l_J/2)^3$ is the Jeans mass, and $t_{\text{ff}} = \sqrt{3\pi/(32G\rho)}$ is the free-fall time (Shu 1977; Stahler et al. 1986). Since the sound speed is higher at lower metallicity, the mean accretion rate onto the protostar \dot{M}_* is also higher in our cases, because \dot{M}_* is roughly proportional to \dot{M}_{infall} . The mass of the central star is consequently higher at lower metallicity at a given epoch. In fact, at the snapshots of $t = 15$ kyr presented in Figure 2, the central stellar mass is $28 M_\odot$ for $0 Z_\odot$, while it is only $0.11 M_\odot$ for $1 Z_\odot$.

Figure 3 shows the spatial distributions of the gas temperature at the same epoch as in Figure 2. As with the surface density, we also find significant differences in the temperature structure among the models. The temperature tends to be higher for lower metallicity because the cooling becomes less efficient. At metallicities of 1 and $0.1 Z_\odot$, the dust cooling is efficient everywhere within the regions presented in the panels. The energy transferred from the gas to dust via collisions is dissipated by the dust thermal emission (Equation 12). In the envelope where the density is relatively low $< 10^6 \text{ cm}^{-3}$, the temperature is ~ 10 K because of such efficient cooling (see also Figure A1). The temperature slightly rises to ≈ 30 – 100 K within ~ 100 au around the central star because the stellar irradiation is effective in addition to the compressional heating (see also Section 4.1 for more details). At $\leq 10^{-2} Z_\odot$, the dust cooling becomes inefficient in the accretion envelope, where the temperature is mostly determined by the thermal balance between the energy loss by molecular-line emission and the compressional heating. The envelope temperature at $\leq 10^{-2} Z_\odot$ is higher (> 100 K) than that at $\geq 0.1 Z_\odot$ as shown in Figure 3. In the cases of $\leq 10^{-2} Z_\odot$, the dust cooling becomes effective only in dense disc materials near the star,

where frequent gas-dust collisions occur. As a result, dense structures such as spiral arms with $\sim 10^8$ – 10^{12} cm^{-3} are colder than in the accretion envelope. The threshold density above which the dust cooling is efficient increases with decreasing metallicity. The region where the dust is the primary coolant gradually shrinks and becomes limited to very vicinity of the central star. Eventually, at $\leq 10^{-6} Z_\odot$, the dust cooling is no longer effective, and the energy loss by H_2 molecular emission dominates everywhere in the computational domain. At these metallicities, the disc temperature is the highest ($> 10^3$ K) among the models.

To examine physical properties of the clumps observed in the simulations quantitatively, we present their mass distribution at $t = 15$ kyr in Figure 4. We describe the method to identify self-gravitating clumps separately in Appendix B. Figure 4 shows that the number of clumps is only 1–2 for $1 Z_\odot$ and $10^{-1} Z_\odot$, while it is as large as ~ 10 – 20 for $\leq 10^{-2} Z_\odot$. We also show the metallicity dependence of the clump number over a longer duration 10–15 kyr in Figure 5a. We see the same overall trend as in Figure 4: the clump number is highest for the cases of 10^{-2} – $10^{-5} Z_\odot$, and the maximum mean value is ~ 15 . Note that the clump number varies by almost an order of magnitude during the 5-kyr duration in these cases, as a result of clump merging, migration toward the star and local fragmentation. In Figure 4, for instance, the number of clumps at $10^{-4} Z_\odot$ is significantly less than those for the adjacent 10^{-3} and $10^{-5} Z_\odot$ cases. However, Figure 5a illustrates that this is just a transient phenomenon. Figure 5a also shows that the number of clumps decreases for $\geq 10^{-2} Z_\odot$ and $\leq 10^{-5} Z_\odot$ toward both the low- and high-metallicity ends. Nevertheless, the decrease at $\leq 10^{-6} Z_\odot$ is modest, and the time-averaged value is no less than ~ 10 .

Figure 4 suggests that not only the number of clumps but also their mass distribution depends on the metallicity: the typical clump mass increases with decreasing metallicity¹. At the metallicity of 1 and $0.1 Z_\odot$, the median clump mass is $M_{\text{c,med}} < 10^{-2} M_\odot$, while it

¹ Figure 4 also suggests that the minimum clump mass increases with de-

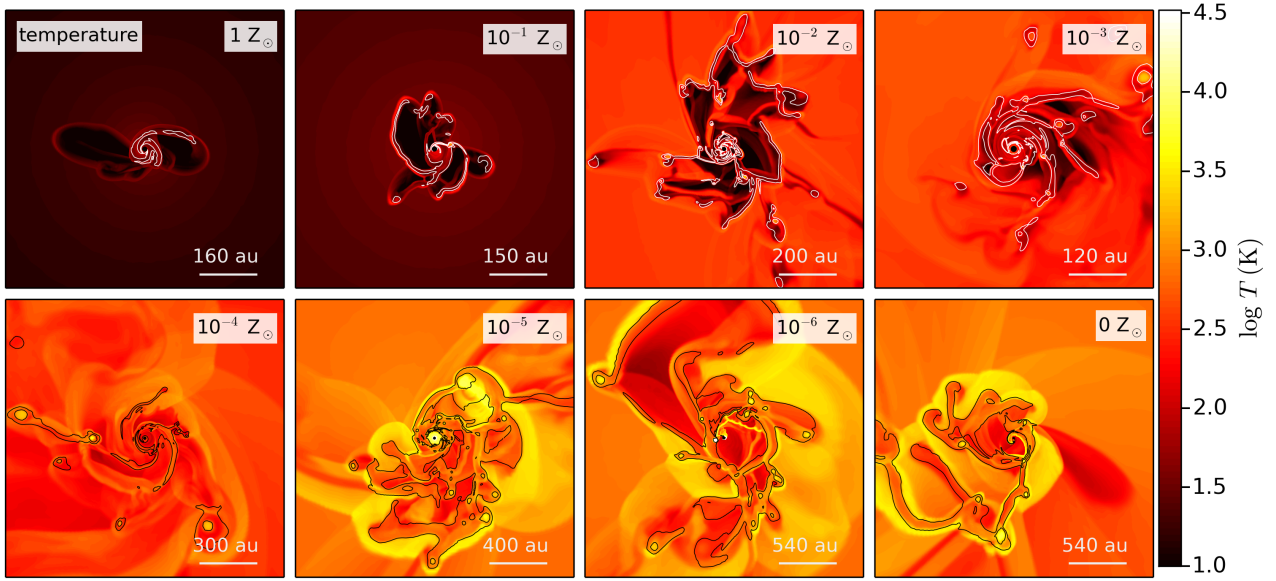


Figure 3. Same as Figure 2 but for the spatial distributions of the gas temperature. The contour lines indicate iso-surface-density lines with $\log(\Sigma/\text{g cm}^{-2}) = 1.5$ and 3.0 (white in top panels, and black in bottom panels).

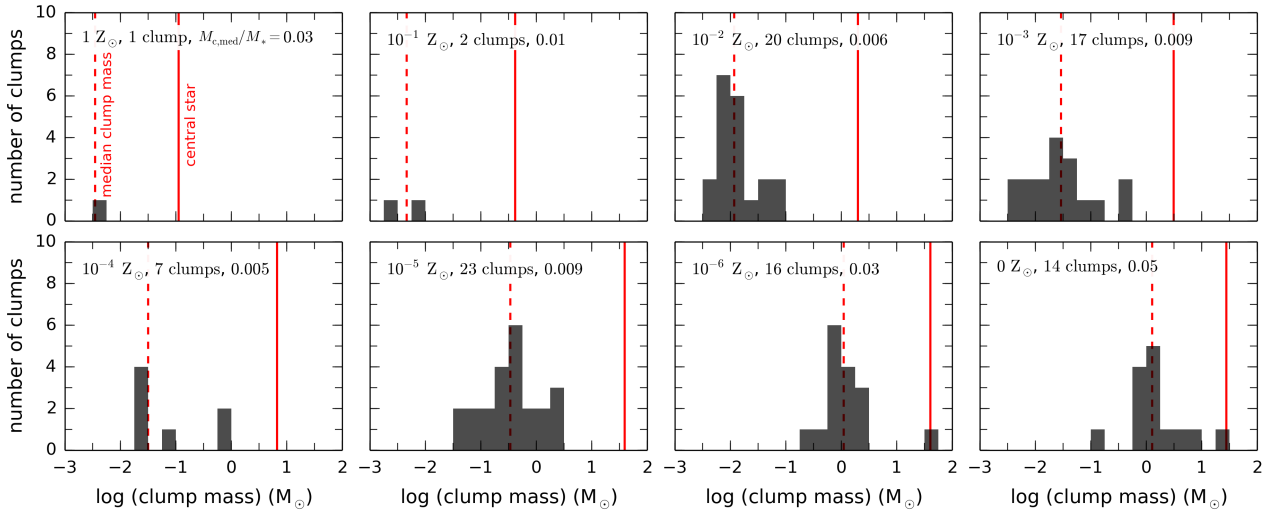


Figure 4. Mass distribution of clumps at 15 kyr elapsed from the disc formation. The panels depict models with different metallicities indicated on the upper-left corners. In each panel, the red vertical lines represent the central stellar mass M_* (solid) and the median mass of clumps $M_{c,med}$ (dashed). The number of clumps and the ratio of the median mass to the central stellar mass are presented in the upper part of each panel.

exceeds $10^{-2} M_{\odot}$ at $\approx 10^{-2} Z_{\odot}$ and rises to $\sim 1 M_{\odot}$ for $\lesssim 10^{-6} Z_{\odot}$. While the overall trend is similar to the metallicity dependence of the central stellar mass, the median clump mass is generally smaller than the central stellar mass by more than one order of magnitude. The contrast is particularly large for 10^{-2} – $10^{-4} Z_{\odot}$, where the number of clumps is largest. The median clump mass is more than two orders of magnitude smaller than the stellar mass for these cases. From $1 Z_{\odot}$ toward lower metallicities, the median clump mass does not vary much from $\sim 10^{-2} M_{\odot}$ until $\sim 10^{-4} Z_{\odot}$, while the central stellar

mass monotonically shifts to a larger value. We investigate the cause of this trend in Section 3.1.2.

3.1.2 Metallicity dependence of typical clump mass

Recent theoretical studies show that the fragmentation of spiral arms is essential in driving the disc fragmentation (e.g. Takahashi et al. 2016; Brucy & Hennebelle 2021). To understand the metallicity dependence of the typical clump mass, we consider the gas thermal evolution during the fragmentation of a spiral arm, and its metallicity dependence. Figure 6 shows gas thermal states of dense parts of spiral arms on the n - T plane, where the fragmentation is about to take place for 1 , 10^{-3} , and $0 Z_{\odot}$. As shown in the right panels, we pick up

creasing metallicity, consistent with analytical argument on the gas giant planet formation via disc fragmentation by Johnson & Li (2013).

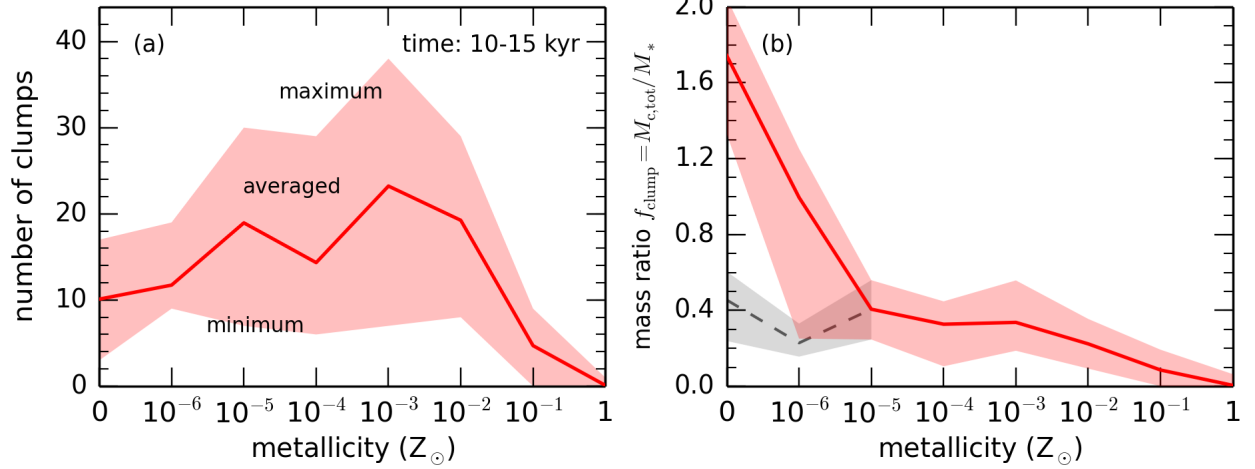


Figure 5. Metallicity dependence of (a) the number of clumps and (b) the mass ratio f_{clump} , i.e. the ratio of the sum of all clump masses $M_{\text{c,tot}}$ to the central stellar mass M_* , at 10–15 kyr from the disc formation. In both panels, the solid red line represents the time-averaged value over 10–15 kyr, and the red shaded area depicts the range over which the quantities vary within the period. In panel (b), the black dashed line and grey shaded area represent the cases where the most massive clump is regarded as a part of the central star. That is, f_{clump} is redefined as $(M_{\text{c,tot}} - M_{\text{c,massive}}) / (M_* + M_{\text{c,massive}})$, where $M_{\text{c,massive}}$ is the mass of the most massive clump (also see the text).

spiral arms that are somewhat isolated because numerous spiral arms form an intricate structure near the centre. Indeed, fragmentation is prone to occur in such outer disc parts, in agreement with studies on fragmentation of solar-metallicity discs (Vorobyov & Basu 2015).

We confirm in those regions the conditions for the disc fragmentation are satisfied; $Q_T < 1$ (Toomre 1964) and $\mathcal{G} < 2/[75\gamma(\gamma - 1)]$ (Gammie 2001; Rice et al. 2005), for which the Toomre parameter Q_T and the normalized cooling time \mathcal{G} are defined as

$$Q_T = \frac{c_s \Omega}{\pi G \Sigma}, \quad (20)$$

$$\mathcal{G} = t_{\text{cool}} \Omega, \quad (21)$$

where Ω is the Kepler angular velocity and $t_{\text{cool}} = e/Q_{\text{tot}}$ is the cooling time. In the insets of the right panels we can see that both these conditions are satisfied in the fragmenting spiral arms.

In the left panel, the grey shaded area represents the state where the gas and dust temperatures well couple in a gravitationally collapsing cloud (Tanaka & Omukai 2014):

$$T < 49 \left(\frac{n_{\text{H}}}{10^{10} \text{ cm}^{-3}} \right)^{2/9} \text{ K}. \quad (22)$$

The collisional energy exchange between gas and dust becomes effective as the thermal state approaches this area. If the local density in the spiral arm becomes high enough to enter in the shaded area, the dust cooling affects the gas thermal state significantly.

First, at $1 Z_{\odot}$ (green circles), all the data plots are within the shaded area, suggesting the efficient gas-dust energy exchange and then the dust cooling throughout the fragmentation process. The temperature is almost constant at ≈ 20 – 30 K for the density of $\lesssim 10^{11} \text{ cm}^{-3}$ and rises with the density for $\gtrsim 10^{11} \text{ cm}^{-3}$. This temperature rise indicates that dust cooling becomes inefficient owing to enhanced optical depth, and the gas thermal evolution becomes adiabatic. The threshold density of $\sim 10^{11} \text{ cm}^{-3}$ nearly corresponds to that for the so-called first hydrostatic cores (or Larson’s first cores) in the present-day star formation (Larson 1969; Omukai 2007; Tomida et al. 2010; Saigo & Tomisaka 2011).

Next, at $10^{-3} Z_{\odot}$ (blue squares), the temperature drops from \approx

200 K to 60 K as the density increases from 10^{10} to 10^{12} cm^{-3} . A striking feature of this case is that the data plots approach the shaded area with increasing density. The dust cooling is inefficient for $< 10^{10} \text{ cm}^{-3}$, where the energy loss by molecular-line emission is the main cooling process. However, dust cooling becomes more and more effective as the density increases, so the temperature substantially decreases. After entering the shaded area for $\gtrsim 2 \times 10^{11} \text{ cm}^{-3}$, the temperature turns to increase again. This occurs because, as in the case of $1 Z_{\odot}$, the dust radiative cooling becomes less effective owing to the photon trapping effect (Tanaka & Omukai 2014). For this case, the gas distribution on the n - T plane is the same as supposed for the so-called dust-induced fragmentation in the extremely metal-poor star formation (e.g. Omukai et al. 2010). Basically the same mechanism is responsible for the disc fragmentation.

Finally, at $0 Z_{\odot}$ (orange triangles), the data plots scatter in the upper part with $T \sim 10^3$ K above the shaded area. With no dust grains in the primordial case, H_2 molecules are the dominant coolant for all the points. We see that the temperature increases above $\sim 10^{13} \text{ cm}^{-3}$ to reach $T \approx 5000$ K. However, such behaviour is likely to be an artefact caused by our limited spatial resolution, rather than the photon trapping effect. We discuss this later in Section 4.2.

As shown above, Figure 6 suggests that thermal evolution during the fragmentation of the arms varies with different metallicities. If the spiral-arm fragmentation is approximated as filament fragmentation, the Jeans mass at the local minimum on the n - T plane should appear as a characteristic scale because the critical effective adiabatic index above that further contraction of filaments is prohibited is unity for such configuration. In Figure 6, the densities where the temperature turns to increase again, which are indicated by the arrows, are $\sim 10^{11} \text{ cm}^{-3}$ for $1 Z_{\odot}$, $\sim 5 \times 10^{11} \text{ cm}^{-3}$ for $10^{-3} Z_{\odot}$, and $\sim 10^{13} \text{ cm}^{-3}$ for $0 Z_{\odot}$. The Jeans masses at these points are $\sim 10^{-2} M_{\odot}$ for 1 and $10^{-3} Z_{\odot}$, and $\sim 1 M_{\odot}$ for $0 Z_{\odot}$. These values explain well the metallicity dependence of the median clump masses shown in Figure 4.

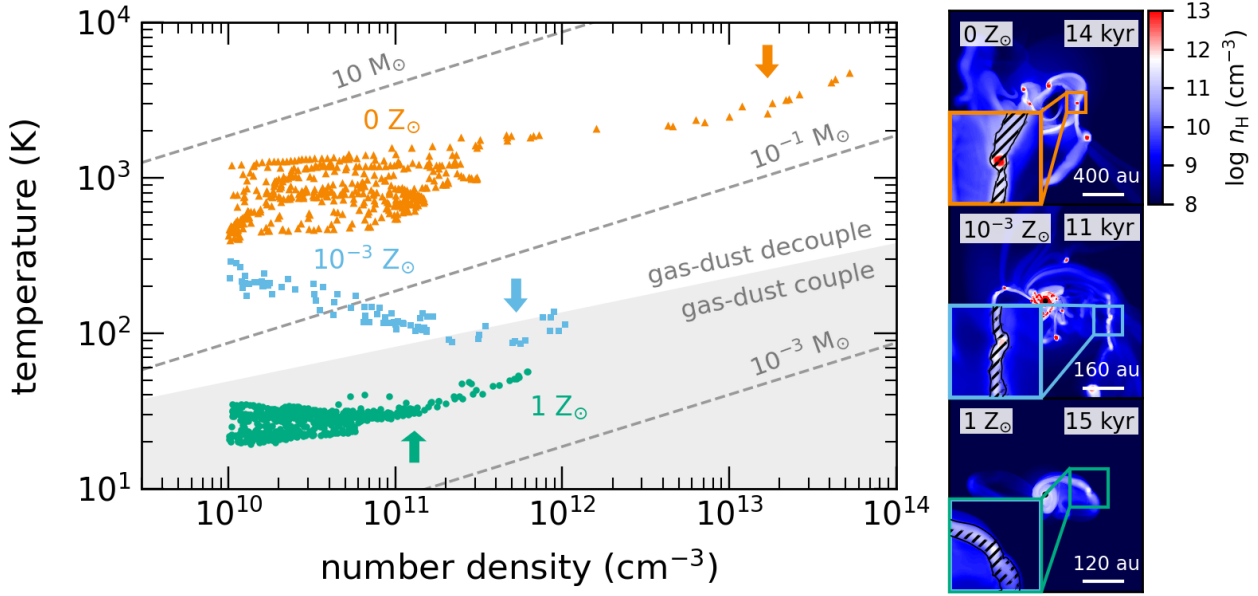


Figure 6. *Left panel:* Metallicity dependence of the gas thermal state of the clumps forming in spiral arms and their surroundings. The colours of the data points represent different metallicities, $1 Z_{\odot}$ (green circles), $10^{-3} Z_{\odot}$ (blue squares), and $0 Z_{\odot}$ (orange triangles). The grey dashed line is the equal Jeans mass line, and the grey shaded area represents the state where the gas and dust temperature couple (also see text). The arrows indicate the temperature turning points at which the Jeans mass is estimated. *Right panels:* Snapshots of the number density distribution at the same epochs displayed in the left panel. The metallicity and elapsed time at which the snapshot is taken are shown at the top of each panel. A magnified view around the clump is depicted in the lower-left corner of each panel. The area surrounding the clump with a number density of $> 10^{10} \text{ cm}^{-3}$ corresponds to the gas whose thermal state is displayed in the left panel. The black line marks the boundary of the region with the Toomre parameter $Q_T < 1$, and in the hatched regions the fragmentation criteria are satisfied; i.e., both $Q_T < 1$ and $\mathcal{G} < 2 [75\gamma(\gamma - 1)]$, where \mathcal{G} is the normalized cooling time (see Equations 20 and 21).

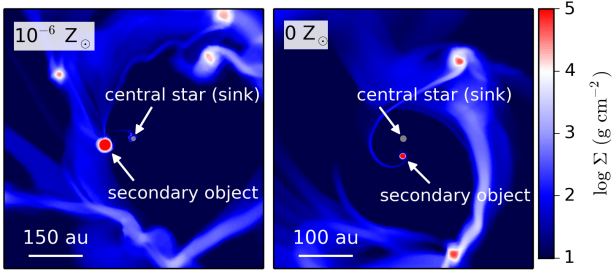


Figure 7. Enlarged views near the central star for the cases of $10^{-6} Z_{\odot}$ (left) and $0 Z_{\odot}$ (right). The panels show the spatial distributions of the surface density over much smaller areas than in Figure 2. The arrows mark the central star and most massive clump found in the snapshots. They are equally massive, forming long-lasting binary systems.

3.1.3 Metallicity dependence of the clump number

We interpret the metallicity dependence of the clump numbers (Figure 5a) based on our consideration in Section 3.1.2. For this purpose, we investigate the total mass of all the clumps $M_{c,\text{tot}}$. Figure 5b shows the metallicity dependence of the mass ratio defined as $f_{\text{clump}} = M_{c,\text{tot}}/M_*$. From Figure 5b, we see that f_{clump} is larger at lower metallicities. The mass ratio f_{clump} is smaller than 0.1 at $1-0.1 Z_{\odot}$ because only a few clumps form. At $10^{-2}-10^{-5} Z_{\odot}$, where the fragmentation is intense, f_{clump} is almost constant at $\approx 0.2-0.4$. At 10^{-6} and $0 Z_{\odot}$, f_{clump} is apparently higher (> 1.0) than at higher metallicities. However, these are peculiar cases as shown in Figure 7: a clump as massive as the central star orbits around the

central star in the small separations of $< 100 \text{ au}$. The most massive clump, i.e., the secondary object, accretes the gas at a higher rate than the central star after its emergence (see also Section 3.2) and stays in a stable orbit for a long period. Compared to the other clumps, the secondary object is unique and should be treated in the same way as the central star. We accordingly redefine f_{clump} as $(M_{c,\text{tot}} - M_{c,\text{massive}})/(M_* + M_{c,\text{massive}})$ only for these cases, where $M_{c,\text{massive}}$ is the mass of the secondary object. Figure 5b shows that with the new definition $f_{\text{clump}} \approx 0.2-0.5$ at 10^{-6} and $0 Z_{\odot}$ (grey filled region), which are comparable to the values for $10^{-2}-10^{-5} Z_{\odot}$. In other words, f_{clump} is nearly constant regardless of the metallicity for the cases of $\leq 10^{-2} Z_{\odot}$, where the disc fragmentation forms more than ten clumps.

Recall that the median clump mass $M_{c,\text{med}}$ is the smallest against the central stellar mass M_* for the cases of $10^{-2}-10^{-4} Z_{\odot}$ (Figure 4). Since the mass ratio f_{clump} is nearly constant as shown in Figure 5b, the median clump mass $M_{c,\text{med}}$ is smallest relative to the clump total mass $M_{c,\text{tot}}$ for these cases. Therefore, the number of clumps $\sim M_{c,\text{tot}}/M_{c,\text{med}}$ is largest at these metallicities, the trend shown in Figure 5a. The above discussion suggests that the slight decline of the clump number at $\leq 10^{-5} Z_{\odot}$ (Figure 5a) is due to the increase of the typical clump mass. As mentioned above, however, this is likely an artificial trend caused by the limited spatial resolutions (see also Section 4.2).

3.2 Disc fragmentation in early period before 10 kyr

Section 3.1 has described the disc fragmentation from 10 to 15 kyr after the disc formation. Next, we investigate the clump number and

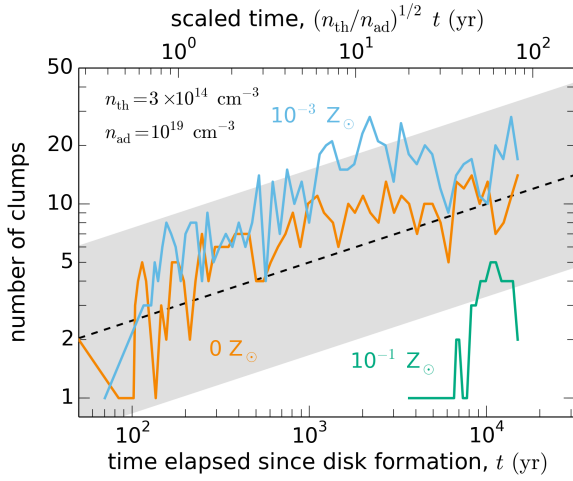


Figure 8. Metallicity-dependent evolution of the number of clumps for 15 kyr after the epoch of disc formation. The line colours represent different metallicities, 10^{-1} (green), 10^{-3} (blue), and $0 Z_{\odot}$ (orange). The lower and upper horizontal axes are the elapsed time since the disc formation and the time normalized as $\sqrt{n_{\text{th}}/n_{\text{ad}}} t$, where $n_{\text{th}} = 3 \times 10^{14} \text{ cm}^{-3}$ and $n_{\text{ad}} = 10^{19} \text{ cm}^{-3}$. The black dashed line represents the scaling relation Equation (23) given by Susa (2019). The grey shaded area denotes the range bounded by 3 and $1/3$ times the black dashed line, where previous simulation results of the primordial star formation distribute (Susa 2019).

accretion rates onto the central star, including the earlier epoch than $t = 10\text{--}15$ kyr.

3.2.1 Number of clumps increasing or decreasing with time

Figure 8 shows the time evolution of the number of clumps for the cases of 10^{-1} , 10^{-3} , and $0 Z_{\odot}$. Even in the early stage of $t < 10$ kyr, the metallicity dependence of the clumps number is almost the same as in Figure 5a. The clump number at $10^{-1} Z_{\odot}$ is always the smallest among those three cases. The first clump appears late at ≈ 3 kyr, and the clump number is five even at the maximum. In contrast, at 10^{-3} and $0 Z_{\odot}$, the first clump appears shortly (< 100 yr) after the disc formation, and then the clump number continuously increases to $\sim 10\text{--}20$ with some oscillation in number.

As shown in Figure 6, at metallicities 1 and $10^{-3} Z_{\odot}$, our simulations resolve characteristic densities above which the gas becomes optically thick and adiabatic, i.e. $n_{\text{ad}} \sim 10^{11}\text{--}10^{12} \text{ cm}^{-3}$. At $0 Z_{\odot}$, however, the gas becomes adiabatic at a very high density of 10^{19} cm^{-3} (e.g. Omukai & Nishi 1998), which is unresolved in most simulations of the disc fragmentation, including ours (see Figure 6). One must be careful when comparing the simulation results with different resolutions. Previous studies show that lower resolution leads to less disc fragmentation and fewer clumps with higher masses because the threshold density above which the gas becomes adiabatic is lower than $\sim 10^{19} \text{ cm}^{-3}$ in a resolution-dependent way. Nonetheless, Susa (2019) found an empirical relation between the clump number N_c and the time elapsed since the protostar formation Δt :

$$N_c \approx 3 \left[\sqrt{\frac{n_{\text{th}}}{n_{\text{ad}}}} \left(\frac{\Delta t}{1 \text{ yr}} \right) \right]^{0.3}, \quad (23)$$

which integrates previous simulation results with different resolutions. The threshold n_{th} represents the density at the resolution limit. For our simulations, we estimate $n_{\text{th}} = 3 \times 10^{14} \text{ cm}^{-3}$, with which the Jeans length assuming $T = 10^3 \text{ K}$ becomes equal to the sink

radius, following Susa (2019). We compare our result of $0 Z_{\odot}$ to Equation (23), using the time measured from the disc formation t for Δt . Figure 8 shows that our result agrees with Equation (23) quite well, supporting the argument by Susa (2019). We can see similar evolution also in our case of $10^{-3} Z_{\odot}$, with always slightly high values. We further discuss our results, comparing them with previous studies in Section 4.4.

3.2.2 Mass accretion histories onto the central star

Figure 9 shows the time evolution of the mass accretion rates onto the central star until $t = 15$ kyr for the different metallicities. As mentioned in Section 3.1.1, the time-averaged accretion rate is higher for lower metallicities: whereas the mean rate is $\sim 10^{-5} M_{\odot} \text{ yr}^{-1}$ at $1 Z_{\odot}$, it is $\sim 10^{-3} M_{\odot} \text{ yr}^{-1}$ at $10^{-5} Z_{\odot}$.

In Figure 9, there are spiky features over a short period of $\ll 1$ kyr in all the cases. These violent fluctuations reflect temporary changes in the accretion rate due to the infall of clumps onto the central star. The frequency of these spiky fluctuations correlates with the number of clumps. For instance, the frequency increases as the metallicity decreases from $1 Z_{\odot}$ while the number of clumps increases. The typical amplitude of the fluctuations also increases with decreasing metallicity: whereas there are only mild fluctuations for $1\text{--}0.1 Z_{\odot}$, the accretion rate more vigorously varies for $\lesssim 10^{-2} Z_{\odot}$.

The presence of clumps also causes long-term variability of the accretion rate over more than kyr, which is particularly noticeable for the cases of 10^{-6} and $0 Z_{\odot}$. In these cases, the accretion rate onto the central star substantially drops at $t \approx 10$ kyr for $10^{-6} Z_{\odot}$ ($t \approx 7$ kyr for $0 Z_{\odot}$), and it stays at the low values after that. The formation of the massive secondary object illustrated in Figure 7 causes such evolution. The secondary object has the typical fragment mass of $\sim 1 M_{\odot}$ at its birth (Section 3.1.2), and it grows comparably massive to the central star ($\sim 25\text{--}30 M_{\odot}$) by accreting the gas from the envelope exclusively. As a result, the accretion rate onto the central star stays low during that period.

In Figure 9, the accretion rate significantly varies by about three orders of magnitude for a few kyr around $t = 10$ and 13 kyr at 10^{-3} and $10^{-4} Z_{\odot}$, respectively. In these cases, the infalling gas temporarily accumulates at a region in the envelope with a density of $\sim 10^6\text{--}10^7 \text{ cm}^{-3}$. Figure A1 shows that efficient H_2 -formation heating creates pressure excess around that part, which decelerates the infall motion (Omukai et al. 2010). We can also confirm this effect from Figure 1b, where the surface density sharply changes at a radius of $\approx 2000\text{--}4000$ au for these metallicity cases. The accumulated gas falls again toward the centre in a free-fall manner after the density is elevated to $\sim 10^8 \text{ cm}^{-3}$. The corresponding free-fall timescale is $\approx 4 (n_{\text{H}}/10^8 \text{ cm}^{-3})^{-1/2} \text{ kyr}$, which is comparable to the timescale of the accretion-rate variation seen in Figure 9. The mass supply rate from the envelope to the disc fluctuates on the free-fall time, and the accretion rate onto the central star is also variable.

4 DISCUSSION

4.1 Effects of protostellar irradiation

Our simulations incorporate the effect of stellar irradiation heating, which has often been neglected in previous studies. In general, irradiation heating is more effective for higher-metallicity discs where the temperature is lower owing to the more efficient dust cooling (Equation 12 and Figure 3), and it works against the disc fragmentation.

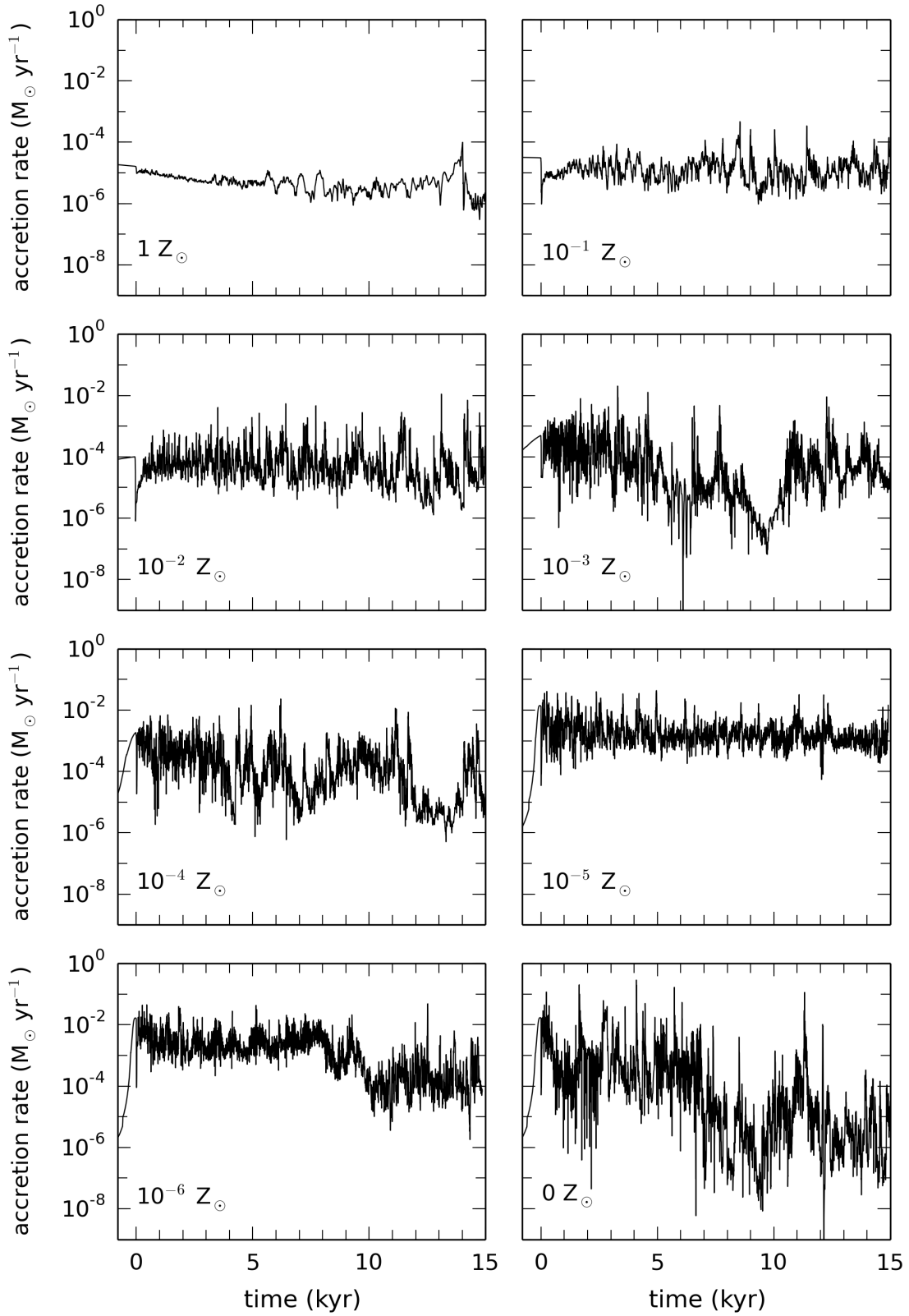


Figure 9. Time evolution of the accretion rate onto the central star from the epoch of disc formation ($t = 0$) to $t = 15$ kyr. The panels represent the cases with different metallicities, as indicated in the lower-left corners of the panels.

As reference models for comparison, we here perform trial simulations ignoring the irradiation heating for the cases of 1 , 10^{-1} , and $10^{-2} Z_{\odot}$. We consider the spatially-uniform background radiation field with 10 K also in these cases. The initial density and angular velocity distributions are the same as in the standard runs described in Section 2.2.

Figure 10 shows the azimuthally-averaged temperature distributions with and without the irradiation heating. For the cases of $1 Z_{\odot}$ and $10^{-1} Z_{\odot}$, the irradiation heating is effective within a radius of ≈ 3000 au from the centre, enhancing the temperature by a factor of a few. At $10^{-2} Z_{\odot}$, the irradiation heating is less prominent than in the above cases and slightly increases the temperature within ~ 100 au from the centre.

Figure 11 illustrates the two-dimensional spatial distributions of the temperature in the same cases. We clearly see that the stellar irradiation increases the temperature in the envelope and disc in the cases of $1 Z_{\odot}$ and $10^{-1} Z_{\odot}$. By contrast, at $10^{-2} Z_{\odot}$, its effect is less evident, affecting only the inner part of the disc. Figure 11 also reveals that the irradiation heating stabilizes the disc and reduces the number of clumps, as reported by Bate (2012) and Stamatellos et al. (2012) for solar-metallicity discs. This effect is particularly remarkable for the cases with 1 and $10^{-1} Z_{\odot}$. Without stellar irradiation, the number of clumps increases by a factor of about three. On the other hand, at $10^{-2} Z_{\odot}$, where the temperature change is small, the difference in the number of clumps is also modest, with only 1.6 times.

While the stellar irradiation affects the disc fragmentation, it only plays a secondary role in shaping the overall metallicity dependence shown in Figure 5a. Even without the stellar irradiation, the number of clumps decreases with increasing metallicity from $10^{-2} Z_{\odot}$ (Figure 11), which is the same trend as in Figure 5a. The irradiation heating effectively stabilizes the disc at higher metallicities, and thus causes the clump number to depend more strongly on the metallicity.

4.2 Limitation by spatial resolution and in search of “true” clump numbers

As described in Section 2.1, we artificially suppress the cooling rate in our simulations (Equation 14). While this method can prevent spurious fragmentation in under-resolved regions, there is a pitfall: it potentially introduces resolution dependencies in the results. We must be careful. Calculations with sufficiently high resolution should mitigate such dependencies, but achieving it for all the cases is computationally infeasible. Hence, we here perform additional simulations only for representative cases 1 and $10^{-3} Z_{\odot}$ to examine the effect of the limited spatial resolution on disc fragmentation. While we have used 512^2 grid cells for the standard runs described in Section 3, we here also examine the runs with 256^2 , 768^2 , and 1024^2 cells. We follow the evolution for 15 kyr after the disc formation for all the additional runs.

Figure 12 shows variations of the clump number with different spatial resolutions. We only see little resolution dependence for the cases of $1 Z_{\odot}$: the disc fragmentation hardly occurs even if we vary the resolution. However, the cases of $10^{-3} Z_{\odot}$ show a large variation with the different resolutions. At this metallicity, the number of clumps monotonically rises from ~ 5 to ~ 40 as the grid number increases from 256^2 to 768^2 . The results with 768^2 and 1024^2 cells are almost the same. Figure 12 thus suggests that our standard run with 512^2 cells underestimates the clump number at $10^{-3} Z_{\odot}$. Recall that the number of clumps tends to increase with decreasing metallicity from 1 to $10^{-3} Z_{\odot}$ (Figure 5a). Considering the resolution dependence, we expect that the actual metallicity dependence is steeper than that shown in Figure 5a.

Let us consider the reason for the large resolution dependence in the case of $10^{-3} Z_{\odot}$ in Figure 12. As discussed in Section 3.1.2, the gas thermal evolution in a fragmenting spiral arm determines the typical clump mass at each metallicity (Figure 6). The characteristic scale set by the Jeans length at the onset of the adiabatic evolution is smaller at a lower metallicity. For example, it is ~ 10 au scale of the first hydrostatic core at $1 Z_{\odot}$ and $\sim 10^{-2}$ au scale of the protostellar core at $0 Z_{\odot}$. Spatially resolving it becomes more difficult with decreasing metallicity. Note that, although the 512^2 resolution is generally insufficient at $10^{-3} Z_{\odot}$, the fragmenting spiral arm in Figure 6 was sufficiently resolved (e.g. $4x_{\text{grid}} < l_J$), and thus the interpretation given in Section 3.1.1 should be correct.

In the most extreme case of primordial star formation ($0 Z_{\odot}$), the characteristic scale is that of a protostar, which is far below our resolution limit. Thus, we expect stronger resolution dependence in this case than for $10^{-3} Z_{\odot}$ shown in Figure 12. Nonetheless, we can estimate the actual number of clumps N_c using Equation (23): substituting $n_{\text{th}} = n_{\text{ad}} = 10^{19} \text{ cm}^{-3}$ and $\Delta t = 15000 \text{ yr}$, Equation (23) reads $N_c \approx 50$. This is five times larger than that for the primordial case (≈ 10 , see Figure 5a) and slightly greater than that for $10^{-3} Z_{\odot}$ with the resolution of 768^2 cells (Figure 12). Therefore, the moderately decreasing trend of N_c from $10^{-3} Z_{\odot}$ to $0 Z_{\odot}$ (Figure 5a) is likely attributable to the limited spatial resolution. Some flat or slightly increasing trend at $N_c \approx 40\text{--}50$ may replace it in reality.

Even with the limited resolution, we can extract the actual metallicity dependence of the disc fragmentation. In Appendix C, we present additional simulations starting from different initial conditions; rapidly rotating cloud cores (Appendix C1) and massive cores (Appendix C2). Modifying the initial condition results in the change in the radii where fragmentation occurs, which also changes the effects of the spatial resolution as the outer region has the lower resolution in our log-polar coordinate system. Therefore, distinguishing the physical effects of the initial conditions and the numerical limitation of spatial resolution is sometimes difficult. Nonetheless, we can discuss the metallicity dependence of the disc fragmentation for a given initial core model. We show that similar metallicity dependence exists even for the different initial models in Figures C1a and C2a (cf. Figure 5a).

4.3 Long-term evolution for 150 kyr

In Section 3, we have analyzed the metallicity dependence of disc fragmentation, particularly the number of clumps and their mass distribution until 15 kyr. Here, we extend the calculation up to 150 kyr in the same cases of 1 and $10^{-3} Z_{\odot}$ and discuss the metallicity dependence in later evolution. At 150 kyr, more than 65 % of material in the parent cloud still remains in the envelope, which continues to supply the mass to the disc.

Figure 13 shows the time evolution of the number of clumps in those cases for 150 kyr. At 15 kyr, the clump number is ~ 10 times larger with $10^{-3} Z_{\odot}$ than with $1 Z_{\odot}$ (Section 3), but their difference becomes smaller and eventually disappears after ≈ 90 kyr. This apparently seems to indicate that the metallicity dependence of disc fragmentation described in Section 3 is only present in the early evolutionary stage. However, one has to be careful about interpreting the results.

First, at $1 Z_{\odot}$, the first clump appears at ~ 10 kyr, and the number of clumps subsequently increases with some fluctuations. We can interpret this trend as follows. The disc radius becomes larger with time as the specific angular momentum of the infalling gas increases in our setting. As a result, the effect of the stellar irradiation heating becomes less effective at the outer edge of the disc, which is prone to

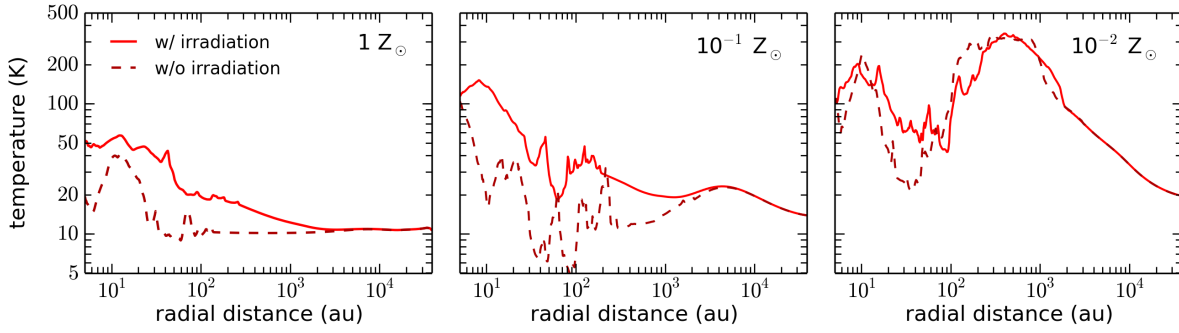


Figure 10. Impact of stellar irradiation heating on the thermal structure of the disc and envelope with different metallicities. The panels show the radial distributions of azimuthally-averaged temperature with different metallicities, 1 (left), 10^{-1} (middle), and $10^{-2} Z_{\odot}$ (right), at the same epoch as in Figure 11. The solid and dashed lines represent the cases with and without the irradiation heating in each panel, respectively.

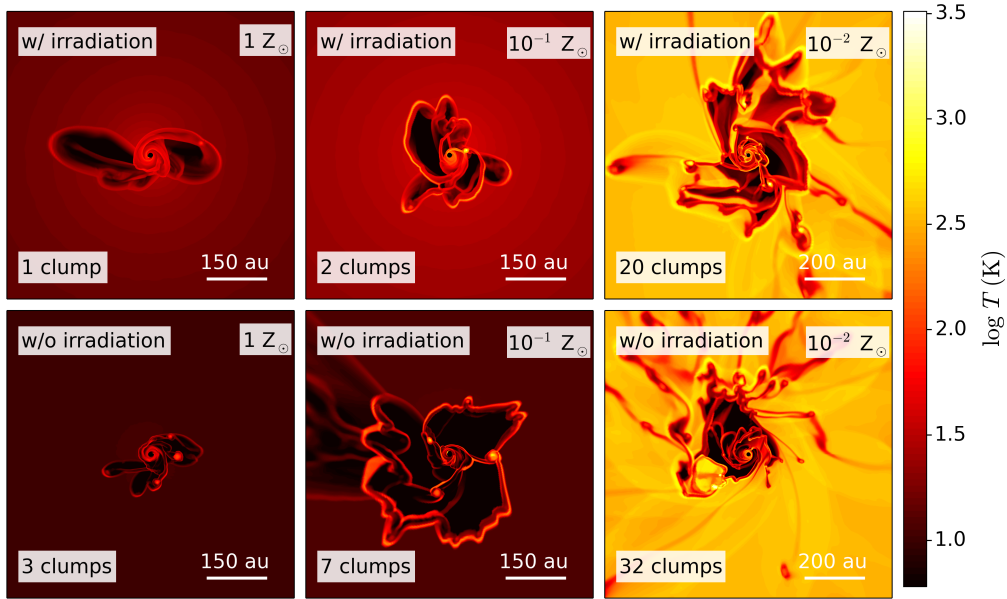


Figure 11. Comparison of the temperature distributions around the central star with and without the central stellar irradiation (upper and lower panels). Each column represent a different metallicity, 1, 10^{-1} , and $10^{-2} Z_{\odot}$, from left to right. All the panels show the snapshots taken at the epoch of 15 kyr after the disc formation. The number of clumps is shown in the lower-left corner of each panel.

fragmentation at ≥ 15 kyr (Section 4.1). In addition, the normalized cooling time \mathcal{G} at the outer edge of the disc tends to be small because of low angular velocity. This promotes fragmentation and then the number of clumps increases (Vorobyov et al. 2020a). Vorobyov & Basu (2010) and Vorobyov et al. (2020a) followed long-term disc evolution at $1 Z_{\odot}$ with very similar code and setting as ours, and reported active disc fragmentation consistent with our result.

Second, at $10^{-3} Z_{\odot}$, dozens of clumps are formed immediately after the disc formation, and the clump number gradually decreases with large fluctuations. This clump-number decline can be interpolated as follows: the density of the disc’s outer edge decreases with time as the disc size extends, and the dust cooling becomes inefficient with $\lesssim 10^{10} \text{ cm}^{-3}$, terminating the fragmentation. However, we must see this result with particular attention to the numerical artefact. As discussed in Section 4.2, the clump number depends on the spatial resolution at $10^{-3} Z_{\odot}$. In the long-term evolution considered here, the disc size becomes larger, and the spatial resolution becomes effectively coarse with time in our log-polar coordinate system. As shown in Figure 12, the lack of resolution leads to underestimating

the clump number, which indicates that the decrease of the clump number at $10^{-3} Z_{\odot}$ shown in Figure 13 is partly due to the insufficient resolution. To confirm how long the metallicity dependence of the disc fragmentation observed in Section 3 persists during the accretion phase, one must systematically perform long-term simulations with sufficiently high resolutions. Such calculations are computationally demanding and outside the scope of this study. It belongs to research in the future world.

4.4 Paying tribute to our predecessors’ achievements

We here compare our simulation results with previous studies. By analyzing the gravitational instability of one-dimensional steady-state discs, Tanaka & Omukai (2014) predicted that vigorous fragmentation occurs at 10^{-3} – $10^{-5} Z_{\odot}$. This is indeed observed in our simulation, and a large number of clumps are produced in this metallicity range, qualitatively consistent with the claim by Tanaka & Omukai (2014).

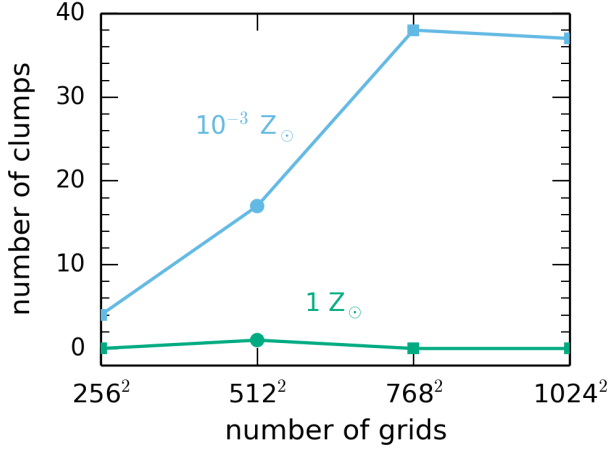


Figure 12. Effect of varying spatial resolution on the number of clumps at $t = 15$ kyr after the disc formation. The circle and square symbols represent the standard cases using 512^2 grid cells and trial cases adopting different resolutions with 256^2 , 768^2 , and 1024^2 cells. The colours indicate different metallicities, 1 (green) and $10^{-3} Z_{\odot}$ (blue).

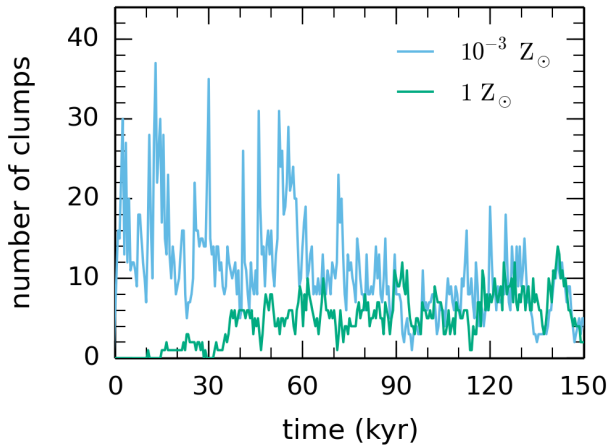


Figure 13. Long-term evolution of the number of clumps for 150 kyr after the disc formation. The green and blue lines show the cases of $1 Z_{\odot}$ and $10^{-3} Z_{\odot}$, respectively.

Intense disc fragmentation at low metallicities is also reported by some other authors who followed shorter-term evolution than ours ($\lesssim 1000$ yr by Machida & Nakamura 2015; Shima & Hosokawa 2021; Chiaki & Yoshida 2022). In their calculation, the number of clumps increases more rapidly than in ours, reaching ~ 10 no later than ~ 100 yr after the birth of the protostar at $\leq 10^{-5} Z_{\odot}$. This can be attributed to the fact that their simulations resolve smaller scales (≤ 10 au) with higher resolution. Our simulations may fail to follow such small-scale fragmentation because of the limited spatial resolution. In our long-term simulations, however, the disc fragmentation occurs in a later phase (> 100 yr) producing ~ 10 clumps. Despite the difference in fragmentation epochs, both results indicate a similar tendency of frequent disc fragmentation at low metallicities.

Some simulations of low-metallicity disc fragmentation followed longer-term evolution ($\sim 10^5$ yr) than ours (Vorobyov et al. 2020b; Chon et al. 2021). They differ from our simulation in terms of the initial conditions, particularly the mass of initial cloud cores. Here,

we vary the core mass as a function of the metallicity, $\approx 3\text{--}1400 M_{\odot}$ for $1\text{--}0 Z_{\odot}$, the typical mass expected at each metallicity. On the other hand, in their studies, the initial mass was fixed in most cases; $\sim 1 M_{\odot}$ for $1\text{--}10^{-2} Z_{\odot}$ in Vorobyov et al. (2020b), and $\sim 1000 M_{\odot}$ for $10^{-1}\text{--}10^{-6} Z_{\odot}$ in Chon et al. (2021). Vorobyov et al. (2020b) adopted a similar prescription as ours, but limited the cases with relatively high metallicity of $\geq 10^{-2} Z_{\odot}$. They show that the violent disc fragmentation continues longer at higher metallicities, by following the long-term evolution until the mass supply from the envelope to the disc ceases. Their results present a similar trend to ours at early phases of $\sim 10^4$ yr after the disc formation. In Chon et al. (2021), at $\leq 10^{-3} Z_{\odot}$ a large number of clumps form in $\sim 10^3$ yr after the protostar formation, similar to our results. Unlike our case, however, they observed a further increase in the clump number at relatively high metallicities of $\geq 10^{-2} Z_{\odot}$. This may be due to Chon et al. (2021)’s omission of the stellar irradiation. Bate (2014, 2019) simulated the star cluster formation with a similar initial condition as in Chon et al. (2021), and reported that the stellar irradiation indeed suppresses low-mass star formation at $\gtrsim 10^{-2} Z_{\odot}$.

5 SUMMARY

We have investigated the metallicity dependence of the circumstellar disc fragmentation by performing two-dimensional radiation-hydrodynamic simulations for a wide range of metallicities $1\text{--}0 Z_{\odot}$. Our simulations follow long-term evolution for 15 kyr and in some models for 150 kyr after disc formation by consistently solving the gas temperature from the energy equation with detailed thermal processes and chemistry network. In this manner, we have properly incorporated disc irradiation heating from an accreting protostar and examined its effect on the disc fragmentation. We have also separately solved gas and dust temperatures, which allows us to accurately follow the dust-induced fragmentation at very low metallicities. Our findings are summarized as follows.

- The disc fragmentation occurs in all the cases we examined by the end of simulations, although its frequency depends on metallicity (Figures 4 and 5). The fragmentation is less frequent at 1 and $10^{-1} Z_{\odot}$, only providing a few clumps in a given moment. At lower metallicities of $\leq 10^{-2} Z_{\odot}$, we have observed intense fragmentation with $\gtrsim 10$ clumps at any time. In particular, the clump number is as high as ≈ 20 at $10^{-2}\text{--}10^{-5} Z_{\odot}$.
- The clump-mass distribution depends strongly on the metallicity. The ratio between the median clump mass and the central stellar mass is remarkably small for the cases of $10^{-2}\text{--}10^{-4} Z_{\odot}$, where the number of the clumps is high. Those low-mass clumps with $\sim 10^{-2} M_{\odot}$ are produced by the fragmentation of spiral arms in the disc induced by the dust cooling.
- The stellar irradiation heating stabilizes the disc and reduces the clump number, especially at relatively high metallicities of $\gtrsim 10^{-2} Z_{\odot}$. Even without stellar irradiation, the number of clumps tends to decrease with increasing metallicity $\gtrsim 10^{-2} Z_{\odot}$. However, this trend is more pronounced by the irradiation heating, i.e. the irradiation heating strengthens the metallicity dependence of the disc fragmentation.

In our simulations, the number of clumps is underestimated owing to limited spatial resolution, particularly in the cases of the lowest metallicities. At $10^{-3}\text{--}0 Z_{\odot}$, for instance, the number of clumps formed by disc fragmentation can be doubled by improving of the resolution. The actual metallicity dependence of the disc fragmentation should be stronger than in our results. This may explain the

observed high close binary fraction of solar-type stars at low metallicities $-3 < [\text{Fe}/\text{H}] < 0$.

ACKNOWLEDGMENTS

The authors wish to express their cordial gratitude to Prof. Takahiro Tanaka, Leader of Innovative Area Grants-in-Aid for Scientific Research “Gravitational wave physics and astronomy: Genesis”, for his continuous interest and encouragement. The authors also would like to thank Profs. Masashi Chiba, Hidekazu Tanaka, and Kengo Tomida and Drs. Sunmyon Chon and Kazuyuki Sugimura for fruitful discussions and useful comments. The numerical simulations were carried out on XC50 Aterui II in Oshu City at the Center for Computational Astrophysics (CfCA) of the National Astronomical Observatory of Japan, through the courtesy of Prof. Eiichiro Kokubo. This research could never be accomplished without the support by Grants-in-Aid for Scientific Research (KEIT: JP19K14760, JP19H05080, JP21H00058, JP21H01145, KO: 17H06360, 17H01102, 17H02869, 22H00149 TH:17H06360, 19H01934, 21H00041) from the Japan Society for the Promotion of Science. EIV acknowledges support from the Austrian Science Fund (FWF) under research grant P31635-N27. KO acknowledges support from the Amaldi Research Center funded by the MIUR program “Dipartimento di Eccellenza” (CUP:B81I18001170001). We are deeply grateful to all parties involved.

DATA AVAILABILITY

The data underlying this article will be shared on reasonable request to the corresponding author.

REFERENCES

- Bastian N., Covey K. R., Meyer M. R., 2010, *ARA&A*, **48**, 339
- Basu S., 1997, *ApJ*, **485**, 240
- Bate M. R., 2012, *MNRAS*, **419**, 3115
- Bate M. R., 2014, *MNRAS*, **442**, 285
- Bate M. R., 2019, *MNRAS*, **484**, 2341
- Brucy N., Hennebelle P., 2021, *MNRAS*, **503**, 4192
- Chabrier G., 2003, *PASP*, **115**, 763
- Chiaki G., Yoshida N., 2022, *MNRAS*, **510**, 5199
- Chiaki G., Schneider R., Nozawa T., Omukai K., Limongi M., Yoshida N., Chieffi A., 2014, *MNRAS*, **439**, 3121
- Chiaki G., Marassi S., Nozawa T., Yoshida N., Schneider R., Omukai K., Limongi M., Chieffi A., 2015, *MNRAS*, **446**, 2659
- Chiaki G., Yoshida N., Hirano S., 2016, *MNRAS*, **463**, 2781
- Chon S., Omukai K., Schneider R., 2021, *MNRAS*, **508**, 4175
- Clark P. C., Glover S. C. O., Klessen R. S., 2008, *ApJ*, **672**, 757
- Clark P. C., Glover S. C. O., Klessen R. S., Bromm V., 2011, *ApJ*, **727**, 110
- Dopcke G., Glover S. C. O., Clark P. C., Klessen R. S., 2011, *ApJ*, **729**, L3
- Dopcke G., Glover S. C. O., Clark P. C., Klessen R. S., 2013, *ApJ*, **766**, 103
- Federrath C., Sur S., Schleicher D. R. G., Banerjee R., Klessen R. S., 2011, *ApJ*, **731**, 62
- Fukushima H., Hosokawa T., Chiaki G., Omukai K., Yoshida N., Kuiper R., 2020, *MNRAS*, **497**, 829
- Gammie C. F., 2001, *ApJ*, **553**, 174
- Greif T. H., Bromm V., Clark P. C., Glover S. C. O., Smith R. J., Klessen R. S., Yoshida N., Springel V., 2012, *MNRAS*, **424**, 399
- Hirano S., Bromm V., 2017, *MNRAS*, **470**, 898
- Hirano S., Hosokawa T., Yoshida N., Umeda H., Omukai K., Chiaki G., Yorke H. W., 2014, *ApJ*, **781**, 60
- Hirano S., Hosokawa T., Yoshida N., Omukai K., Yorke H. W., 2015, *MNRAS*, **448**, 568
- Hollenbach D., McKee C. F., 1979, *ApJS*, **41**, 555
- Hosokawa T., Omukai K., 2009, *ApJ*, **703**, 1810
- Hosokawa T., Omukai K., Yoshida N., Yorke H. W., 2011, *Science*, **334**, 1250
- Hosokawa T., Hirano S., Kuiper R., Yorke H. W., Omukai K., Yoshida N., 2016, *ApJ*, **824**, 119
- Johnson J. L., Li H., 2013, *MNRAS*, **431**, 972
- Kimura K., Hosokawa T., Sugimura K., 2021, *ApJ*, **911**, 52
- Kratter K., Lodato G., 2016, *ARA&A*, **54**, 271
- Kroupa P., 2002, *Science*, **295**, 82
- Larson R. B., 1969, *MNRAS*, **145**, 271
- Lichtenberg T., Schleicher D. R. G., 2015, *A&A*, **579**, A32
- Machida M. N., Doi K., 2013, *MNRAS*, **435**, 3283
- Machida M. N., Nakamura T., 2015, *MNRAS*, **448**, 1405
- Machida M. N., Omukai K., Matsumoto T., Inutsuka S.-i., 2008, *ApJ*, **677**, 813
- Mathis J. S., Rimpl W., Nordsieck K. H., 1977, *ApJ*, **217**, 425
- Matzner C. D., Levin Y., 2005, *ApJ*, **628**, 817
- McKee C. F., Tan J. C., 2003, *ApJ*, **585**, 850
- McKee C. F., Tan J. C., 2008, *ApJ*, **681**, 771
- Meece G. R., Smith B. D., O’Shea B. W., 2014, *ApJ*, **783**, 75
- Moe M., Kratter K. M., Badenes C., 2019, *ApJ*, **875**, 61
- Omukai K., 2000, *ApJ*, **534**, 809
- Omukai K., 2007, *PASJ*, **59**, 589
- Omukai K., Nishi R., 1998, *ApJ*, **508**, 141
- Omukai K., Tsuribe T., Schneider R., Ferrara A., 2005, *ApJ*, **626**, 627
- Omukai K., Hosokawa T., Yoshida N., 2010, *ApJ*, **722**, 1793
- Prole L. R., Clark P. C., Klessen R. S., Glover S. C. O., 2022, *MNRAS*, **510**, 4019
- Riaz R., Bovino S., Vanaverbeke S., Schleicher D. R. G., 2018, *MNRAS*, **479**, 667
- Rice W. K. M., Lodato G., Armitage P. J., 2005, *MNRAS*, **364**, L56
- Safranek-Shrader C., Montgomery M. H., Milosavljević M., Bromm V., 2016, *MNRAS*, **455**, 3288
- Saigo K., Tomisaka K., 2011, *ApJ*, **728**, 78
- Schlaufman K. C., Thompson I. B., Casey A. R., 2018, *ApJ*, **867**, 98
- Schneider R., Ferrara A., Salvaterra R., Omukai K., Bromm V., 2003, *Nature*, **422**, 869
- Schneider R., Omukai K., Inoue A. K., Ferrara A., 2006, *MNRAS*, **369**, 1437
- Semenov D., Henning T., Helling C., Ilgner M., Sedlmayr E., 2003, *A&A*, **410**, 611
- Shakura N. I., Sunyaev R. A., 1973, *A&A*, **24**, 337
- Sharda P., Federrath C., Krumholz M. R., 2020, *MNRAS*, **497**, 336
- Shima K., Hosokawa T., 2021, *MNRAS*, **508**, 4767
- Shu F. H., 1977, *ApJ*, **214**, 488
- Smith B. D., Wise J. H., O’Shea B. W., Norman M. L., Khochfar S., 2015, *MNRAS*, **452**, 2822
- Stacy A., Greif T. H., Bromm V., 2010, *MNRAS*, **403**, 45
- Stacy A., Bromm V., Lee A. T., 2016, *MNRAS*, **462**, 1307
- Stahler S. W., Palla F., Salpeter E. E., 1986, *ApJ*, **302**, 590
- Stamatellos D., Whitworth A. P., Hubber D. A., 2012, *MNRAS*, **427**, 1182
- Sugimura K., Matsumoto T., Hosokawa T., Hirano S., Omukai K., 2020, *ApJ*, **892**, L14
- Susa H., 2019, *ApJ*, **877**, 99
- Susa H., Hasegawa K., Tominaga N., 2014, *ApJ*, **792**, 32
- Takahashi S. Z., Tsukamoto Y., Inutsuka S., 2016, *MNRAS*, **458**, 3597
- Tanaka K. E. I., Omukai K., 2014, *MNRAS*, **439**, 1884
- Tanaka K. E. I., Tan J. C., Zhang Y., Hosokawa T., 2018, *ApJ*, **861**, 68
- Tomida K., Machida M. N., Saigo K., Tomisaka K., Matsumoto T., 2010, *ApJ*, **725**, L239
- Toomre A., 1964, *ApJ*, **139**, 1217
- Truelove J. K., Klein R. I., McKee C. F., Holliman John H. I., Howell L. H., Greenough J. A., 1997, *ApJ*, **489**, L179
- Vorobyov E. I., Basu S., 2009, *MNRAS*, **393**, 822
- Vorobyov E. I., Basu S., 2010, *ApJ*, **719**, 1896
- Vorobyov E. I., Basu S., 2015, *ApJ*, **805**, 115
- Vorobyov E. I., DeSouza A. L., Basu S., 2013, *ApJ*, **768**, 131

- Vorobyov E. I., Matsukoba R., Omukai K., Guedel M., 2020a, *A&A*, **638**, A102
- Vorobyov E. I., Elbakyan V. G., Omukai K., Hosokawa T., Matsukoba R., Guedel M., 2020b, *A&A*, **641**, A72
- Wollenberg K. M. J., Glover S. C. O., Clark P. C., Klessen R. S., 2020, *MNRAS*, **494**, 1871
- Yorke H. W., Bodenheimer P., 2008, in Beuther H., Linz H., Henning T., eds, *Astronomical Society of the Pacific Conference Series Vol. 387, Massive Star Formation: Observations Confront Theory*. p. 189
- Zhao B., et al., 2020, *Space Sci. Rev.*, **216**, 43

APPENDIX A: THERMAL EVOLUTION

In Section 3.1, we discuss the thermal evolution of the gas, especially focusing only on the circumstellar disc and its surroundings. In this section, we describe the thermal evolution of the cloud as a whole and which cooling process is important in each metallicity.

Figure A1 shows the gas mass distribution on the density-temperature phase diagram. The trend toward higher temperatures for lower metallicities is observed in Figure 3, and it is the same in Figure A1. The gas has the temperature of 10–100 K at $1 Z_{\odot}$, while it has the high temperature of 100–10⁵ K at $0 Z_{\odot}$. This difference in temperature range is due to the variance in the cooling process as explained in Section 3.1.

At $\geq 10^{-1} Z_{\odot}$, the temperature is ~ 10 K at the density of 10^3 – 10^6 cm^{-3} due to the efficient cooling by metal line and dust emission. The temperature increases at higher densities of $\gtrsim 10^6 \text{ cm}^{-3}$ due to the stellar irradiation and the compressional heating (see also Section 4.1).

At $\leq 10^{-2} Z_{\odot}$, the cooling by metal line and dust emission becomes inefficient, resulting in molecular-line emissions as the main cooling process. In this case, the temperature is 30–300 K in the low-density region of 10^3 – 10^6 cm^{-3} . In addition, at 10^{-2} – $10^{-4} Z_{\odot}$, the temperature rises sharply to ~ 500 K at the density of 10^6 – 10^7 cm^{-3} because of the chemical heating associated with the H_2 formation. Then, the temperature peaks at the density of $\sim 10^8 \text{ cm}^{-3}$. At higher densities, the temperature decreases as the dust cooling begins to take effect. This temperature decrease, which is also seen in Figure 6, determines the typical clump mass of $10^{-3} Z_{\odot}$.

At even lower metallicities of $\leq 10^{-6} Z_{\odot}$, the dust cooling does not work, and the gas is cooled by H_2 -line emission in the whole density of 10^3 – 10^{14} cm^{-3} . Since the H_2 -line cooling is less efficient than the dust cooling, the temperature is high, at $\sim 10^3$ K. The hot distribution of $> 10^4$ K in the denser region of $> 10^{14} \text{ cm}^{-3}$ represents the second object seen in Figure 7, where the cooling is artificially suppressed due to the resolution limit (Equation 14).

APPENDIX B: IDENTIFYING SELF-GRAVITATING CLUMPS

Here, we describe the method for identifying clumps from calculation results. We first search for a grid that has a higher surface density than the eight neighbouring grids in the computational domain. We call such a grid the peak grid. The Jeans length λ_J at the peak grid is

$$\lambda_J = 2 \frac{c_{s,\text{peak}}^2}{G \Sigma_{\text{peak}}}, \quad (\text{B1})$$

where $c_{s,\text{peak}}$ and Σ_{peak} are the sound velocity and the surface density at the peak grid. We note that this definition of the Jeans length λ_J is consistent with another definition of l_J in Equation (13) when the gas self-gravity becomes significant. The Jeans radius R_J is half of the

Jeans length, $R = \lambda_J/2$. To ensure that the peak density Σ_{peak} is high enough to qualify as a “clump”, we check the following condition,

$$(i) \Sigma_{\text{peak}} \geq 10 \Sigma_{\text{avr}}, \quad (\text{B2})$$

where Σ_{avr} is the average surface density of the annulus between the radii of R_J and $1.5 R_J$ from the peak grid. If this condition (i) is satisfied, an aggregate of the grids within the Jeans radius of the peak grid is a clump candidate.

Next, we check if the clump candidate is gravitationally bound. Based on the virial analysis, we set the gravitationally-bound condition as

$$(ii) \frac{|E_g|}{2(\gamma - 1)E_{\text{th}} + 2E_{\text{kin}}} \geq 0.6, \quad (\text{B3})$$

where E_g is the gravitational energy, E_{th} is the thermal energy, and E_{kin} is the kinetic energy of the clump candidate. We explored the values on the right-hand side of Equation (B3) between 0.1 and 1.0. Then, we selected the value of 0.6 that can be judged without missing the candidate that is a visually obvious clump. The three energies are given by

$$E_g = - \int \int \frac{1}{2} G \frac{\Sigma \Sigma'}{|\mathbf{r} - \mathbf{r}'|} dS dS', \quad (\text{B4})$$

$$E_{\text{th}} = \int e dS, \quad (\text{B5})$$

$$E_{\text{kin}} = \int \frac{1}{2} \Sigma (\mathbf{u} - \mathbf{u}_c)^2 dS, \quad (\text{B6})$$

where \mathbf{u}_c is the velocity of the mass centre of the clump candidate. The integral range is within the Jeans radius R_J . We declare the clump candidate to be an actual clump if it satisfies the condition (ii).

Some clumps are ejected from the central region due to gravitational interactions with other clumps as well as the central star. Such an ejected clump moves toward the outer region, where the grid is coarser in the spherical coordinate. With insufficient resolution, the density of the ejected clump artificially decreases, reducing its gravitational energy. Consequently, the ejected clump no longer satisfies the gravitationally-bound condition (ii). However, we expect such ejected clumps to keep sufficiently high density in reality. Therefore, we added the following conditions to the clump identification to avoid the omission of counting ejected clumps. Among the candidates satisfying the density condition (i) but not the condition (ii), we certify one as a clump if the speed of the mass centre u_c exceeds the escape velocity from the central stellar gravity u_{esc} , i.e.

$$(iii) u_c > u_{\text{esc}} = \sqrt{2 \frac{GM_*}{r_c}}, \quad (\text{B7})$$

where r_c is the distance between the central star and the mass centre of the candidate. At $t = 15$ kyr from the disc formation (Figure 4), we identified the ejected clumps satisfying the condition (iii) at 10^{-2} , 10^{-3} , 10^{-6} , and $0 Z_{\odot}$, whose ratios are accounted for ~ 20 –40 % of the total clump number.

APPENDIX C: EFFECTS OF VARYING INITIAL PROPERTIES OF STAR-FORMING CLOUDS

We here briefly describe the disc fragmentation in additional simulations starting from different initial cloud core models: rapidly rotating cores (Appendix C1) and massive cores (Appendix C2). As in Section 3, we pay special attention to the number of clumps and the mass ratio f_{clump} .

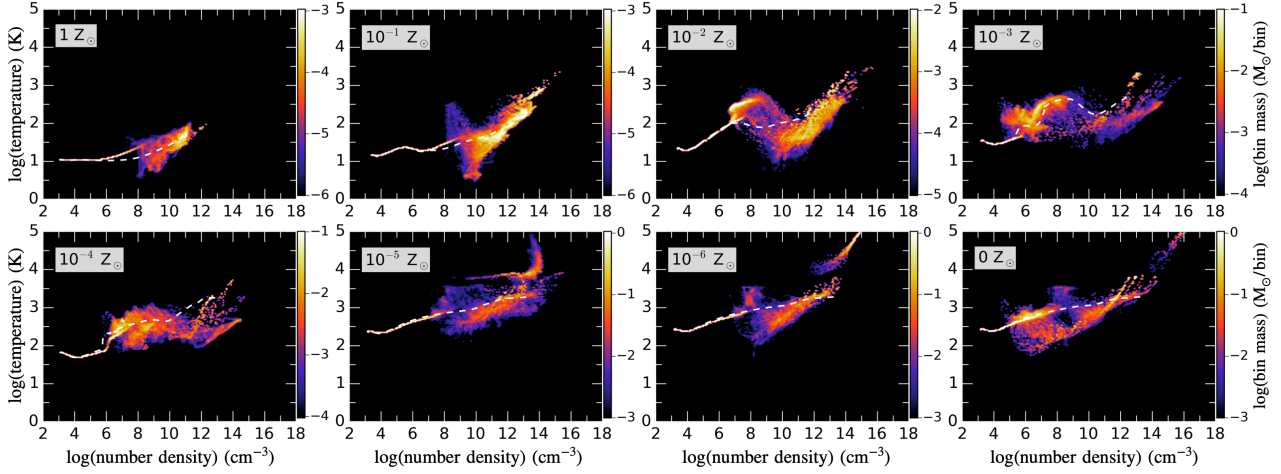


Figure A1. Gas mass distributions on the density-temperature phase diagrams at 15 kyr elapsed from the disc formation. The panels depict models with seven different metallicities shown in the upper left of each panel. The colour indicates the mass in each density-temperature bin with the widths of $\Delta \log(n_{\text{H}}/\text{cm}^{-3}) = 0.1$ and $\Delta \log(T/\text{K}) = 0.03$. The white dashed line is the density-temperature distribution at the disc formation.

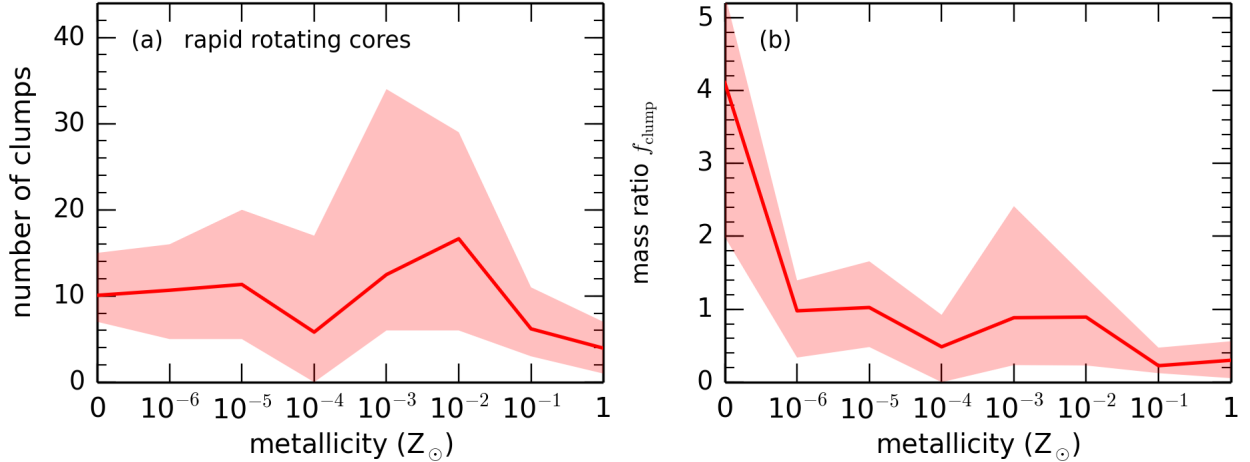


Figure C1. Same as Figure 5 but for the cases starting from the rapidly rotating cores.

C1 rapidly rotating cores

We investigate the cases of “rapidly rotating cores”, for which we assume a higher initial spin than the standard cases described in Section 2.2. While we have assumed the ratio of the rotational and gravitational energies of $\beta = 0.01$ for the standard case, we here consider the cases with $\beta = 0.05$ below. These values are comparable to those assumed in previous studies, $\beta = 0.01$ – 0.02 in Chiaki & Yoshida (2022), and 0.03 – 0.09 in Shima & Hosokawa (2021). The other settings are identical to those used for the standard cases with different metallicities. We follow the evolution for 15 kyr after the disc formation for all the cases.

Figure C1a shows the variations of the clump number with different metallicities for these cases (cf. Figure 5a). We see that the number of clumps is largest at 10^{-2} – $10^{-3} Z_{\odot}$ and it decreases toward both the high- and low-metallicity ends. While the time-averaged clump number has a peak value of ≈ 20 at $10^{-2} Z_{\odot}$, it decreases to a few in the high-metallicity tail of 10^{-1} – $1 Z_{\odot}$. The overall trends are similar to the metallicity dependence of the standard cases (Section 3.1).

Figure C1b shows the metallicity dependence of the mass ratio

f_{clump} , the ratio of the total clump mass to the central stellar mass (cf. Figure 5b). The mass ratio f_{clump} takes the smallest values of ≈ 0.3 at high metallicities 1 and $10^{-1} Z_{\odot}$, and it is nearly constant at 0.5 – 1.0 for the cases of 10^{-2} – $10^{-6} Z_{\odot}$. Only the value at $0 Z_{\odot}$ is remarkably larger than those for the other cases, indicating the formation of a massive secondary clump orbiting around the central star (Figure 7). Again, the overall trend is similar to that for the standard cases (Section 3.1).

It is not straightforward to extract the effects of varying β on the disc fragmentation by comparing Figure 5 and Figure C1 at each metallicity. The higher β results in a larger disc size at a given epoch, leading to effectively poorer spatial resolution in the outer disc, where fragmentation often occurs. Since our simulations tend to underestimate the number of clumps with the lower resolution (Section 4.2), it is tricky to draw out the effect of the initial spin, considering the effect of the different spatial resolutions. We, nonetheless, find no clear and qualitative effects of varying the initial spin on the metallicity dependence of the disc fragmentation.

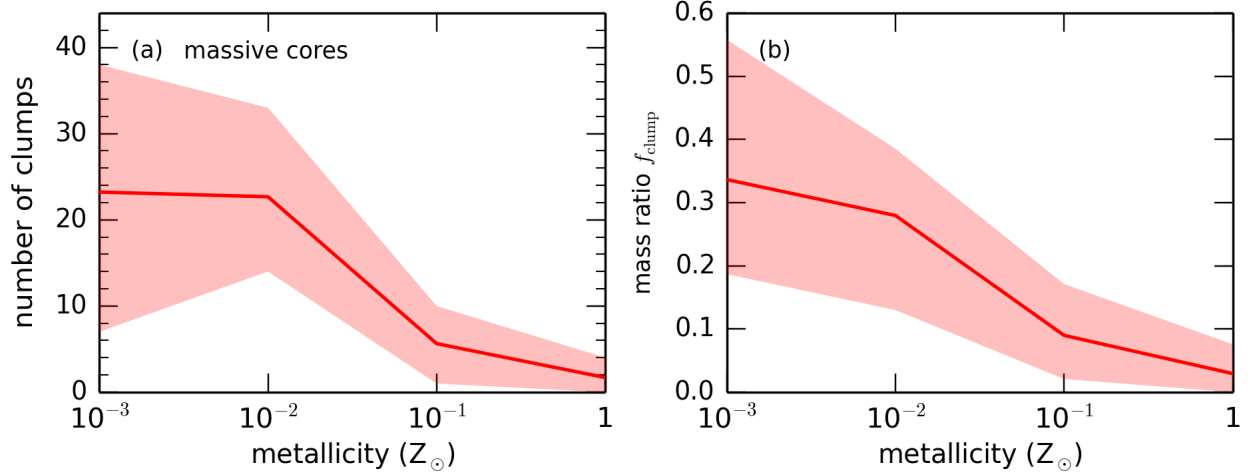


Figure C2. Same as Figure 5 but for the cases starting from the initial massive cores.

C2 massive cores

For our standard cases considered in Section 2.2, we have assumed the less massive initial cores for the higher metallicities, considering the Jeans mass scale given by the gas thermal evolution at each metallicity. In reality, however, the star formation may rarely start with more massive cloud cores than the standard cases, for instance, massive cores supposed for the present-day massive star formation (McKee & Tan 2003). We here perform additional simulations for such rare cases, using the same initial core of $10^{-3} Z_{\odot}$ with $\approx 60 M_{\odot}$ (Table 1) for higher-metallicity cases of 1 , 10^{-1} , and $10^{-2} Z_{\odot}$. The initial mass is ~ 20 times larger than that for the standard case of $1 Z_{\odot}$, $\approx 3.4 M_{\odot}$ (Table 1). We do not consider the cases with $< 10^{-3} Z_{\odot}$, because the initial core mass becomes extremely massive at 100 – $1000 M_{\odot}$, corresponding to cluster-forming clumps at $1 Z_{\odot}$.

Figure C2 shows the metallicity dependencies of the clump number and the mass ratio f_{clump} for these “massive core” cases (cf. Figure 5). The time-averaged number of clumps tends to increase with decreasing the metallicity, from a few at 1 – $10^{-1} Z_{\odot}$ to > 20 at 10^{-2} – $10^{-3} Z_{\odot}$ (Figure C2a). The mass ratio f_{clump} also increases with decreasing the metallicity (Figure C2b). These trends are almost identical to those in Figure 5.

Note that, among the standard cases, the mass-supply rate from the envelope to the disc is significantly lower at the higher metallicities (Section 3). In fact, in Figure 9, the accretion rate to the central star at $1 Z_{\odot}$ is about 10 times smaller than that at $10^{-3} Z_{\odot}$. On the other hand, the accretion rates at 1 and $10^{-3} Z_{\odot}$ in the cases of massive cores are almost the same. Interestingly, even though the accretion rates are not much different among the massive cores, Figure C2 shows the same metallicity dependence as in Figure 5. Tanaka & Omukai (2014) analyzed the disc stability using the one-dimensional steady accretion model, and showed that the disc becomes more stable at higher metallicities in the range of 1 – $10^{-3} Z_{\odot}$, regardless of the prestellar cloud mass. Our results support their prediction.

This paper has been typeset from a \LaTeX file prepared by the author.